Plasma-catalytic dry reforming of CH_4: Effects of plasma-generated species on the surface chemistry

Jintao Sun[1], Qi Chen[1]*, Wanyue Qin[1], Hanyu Wu[2], Bonan Liu[2], Shangkun Li[3], Annemie Bogaerts[3]

1. School of Mechanical, Electronic and Control Engineering, Beijing Jiaotong University, Beijing 100044, China

2. College of Chemical Engineering and Environment, China University of Petroleum-Beijing, Beijing 102249, China

3. Research Group PLASMANT, Department of Chemistry, University of Antwerp, Wilrijk 2610, Belgium

*Corresponding author

E-mail address: qchen@bjtu.edu.cn

Abstract

By means of steady-state experiments and a global model, we studied the effects of plasma-generated reactive species on the surface chemistry and coking in plasma-catalytic CH_4/CO_2 reforming at reduced pressure (8-40 kPa). We used a hybrid ZDPlasKin-CHEMKIN model to predict the species densities over time. The detailed plasma-catalytic mechanism consists of the plasma discharge scheme, a gas-phase chemistry set and a surface mechanism. Our experimental results show that the coupling of Ni/SiO_2 catalyst with plasma is more effective in CH_4/CO_2 activation and conversion than unpacked DBD plasma, with syngas being the main products. The highest total conversion of 16% was achieved at 8000 V and 473 K, with corresponding CO and H_2 yields of 15% and 12%, respectively. The reactants conversion and product selectivity are well captured by the kinetic model. Our simulation results suggest that vibrational species and radicals can accelerate the dissociative adsorption and Eley-Rideal (E-R) reactions. Path flux analysis shows that E-R reactions dominate the surface reaction pathways, which differs from thermal catalysis, indicating that the coupling of non-equilibrium plasma and catalysis can effectively shift the formation and consumption pathways of important adsorbates. For instance, our model suggests that HCOO(s) is primarily generated through the E-R reaction $CO_2(v) + H(s) \rightarrow HCOO(s)$, while the hydrogenation reaction $HCOO(s) + H \rightarrow HCOOH(s)$ is the main source of HCOOH(s). Carbon deposition on the catalyst surface is primarily formed through the stepwise dehydrogenation of CH_4, while the E-R reactions enhanced by plasma-generated H and O atoms dominate the consumption of carbon deposition. This work provides new insights into the effects of reactive species on the surface chemistry in plasma-catalytic CH_4/CO_2 reforming.

Keywords: Dry reforming of methane; Plasma catalysis; Plasma-enhanced surface chemistry; Path flux and sensitivity analysis; Coking kinetics

1. Introduction

Methane (CH_4) and carbon dioxide (CO_2) are the two main greenhouse gases, playing a critical role in global warming and climate change. The chemical transformation of CH_4 and CO_2 into fuels and high-value oxygenates is one of the most promising ways to reduce CO_2 emissions and create a sustainable low-carbon economy [1]. Nevertheless, this dry reforming of methane (DRM; $CH_4 + CO_2 \leftrightarrows 2CO + 2H_2$, $\Delta H^0_{298K} = 247$ kJ/mol) is thermodynamically unfavorable under mild conditions. Conventionally, the traditional thermal catalytic route for syngas production relies on high temperature (> 700 °C) [2,3] to activate the C=O bonds ($E_{diss} = 5.5$ eV) and C-H bonds ($E_{diss} = 4.5$ eV) in CO_2 and CH_4, respectively [4], followed by Fischer-Tropsch synthesis to obtain liquid oxygenates at high pressure. The transition metal Ni catalysts are known as the most representative catalysts for DRM, however, they inevitably leads to catalyst deactivation owing to coke deposition at high temperature. Therefore, a green alternative for DRM at mild operating conditions is urgently needed.

Non-thermal plasma (NTP) is a partially ionized gas, which can generate large amounts of radicals, excited species, photons, ions, and electrons at ambient environment, offering a potential route to overcome the thermodynamic and kinetic limitations in the transformation of reactants into desired products. Moreover, NTP-based

processes are highly adaptable, making them suitable for integration with renewable energy sources like wind and solar power, enabling the decentralized electrification of gas conversion and chemical processes [3]. However, owing to a diverse mixture of highly reactive species present in NTP, it is challenging to attain high selectivity and yield for the desired products. Plasma catalysis, which is the integration of plasma and catalysts, promises to combine the advantages of both, generating the desired products at desired rates and efficiencies that are very difficult or impossible to achieve via conventional catalytic means [5]. Several papers have reported the good performance of plasma catalysis in terms of reactants conversion, energy efficiency or product selectivity, compared to the sum of the individual processes, such as in ammonia synthesis [6-10], CO_2 hydrogenation [11-13], NO_x removal [14], CH_4 oxidation [15,16] and DRM [17-19]. However, improvements in plasma catalysis compared to plasma alone are not always observed, as reported for DRM in a recent review paper [20]. Therefore, comprehending the underlying mechanism into the surface reaction under plasma conditions represents a significant breakthrough toward developing a more efficient plasma-catalytic DRM process. However, plasma catalysis creates a complex environment, as the plasma can affect the catalyst behavior, such as electric field effects, surface charging, hot spot formation, morphological changes and changes in work function of the catalyst, and vice versa, the catalyst can affect the plasma characteristics, potentially leading to plasma-catalyst synergies [21]. Consequently, it is extremely difficult to address the question of how the plasma interacts with the catalyst, and vice versa [20].

From the viewpoint of chemistry, species in vibrationally excited states may experience a lower activation barrier for the dissociation at the surface, while radicals may allow E-R interactions to occur at the catalyst surface, offering additional possible pathways for the chemical conversions. Researchers elaborated on kinetic modelling to tackle the plasma-chemical promotion on catalyst surfaces. Hong et al. [22] first attempted to explore the chemical kinetic modeling of NH_3 synthesis in atmospheric-pressure plasma catalysis. The detailed kinetic mechanism integrated plasma chemistry and heterogeneous surface interactions and was described using the plasma kinetics solver ZDPlasKin [23], providing an innovative approach for the simulation of plasma catalysis using a zero-dimensional (0D) kinetics model. van 't Veer et al. [24] developed an improved model, taking into account the filamentary character of dielectric barrier discharge (DBD) plasmas, and were able to reveal the mechanisms of NH_3 formation and loss (in the gas phase and at the catalytic surface), both during and after the microdischarges. However, both models typically accounted for the adsorption steps and E-R interactions through simple sticking coefficients, which introduces noticeable uncertainty into the rate constants of surface reactions. A significant improvement to such models was introduced by Engelmann et al. [25,26], Michiels et al. [27], Liu et al. [28] and Loenders et al. [29], who applied TST for the calculation of rate coefficients for surface reactions in plasma catalysis, refining the framework of plasma catalysis modeling and enhancing the precision of its parameters. With rate coefficients obtained from TST, they proposed microkinetic models (MKMs) [25-30] incorporating plasma-produced species and surface-adsorbed species to study the mechanisms in plasma catalysis. On top of this, attempts have been made to use density functional theory (DFT) calculations [31] to capture specific influences of the plasma on surface reactions, including surface charging and electric fields at the molecular scale [32]. However, most MKMs (even if they consider the effect of plasma species) and DFT calculations only consider surface reactions in the model and cannot provide a comprehensive description of the plasma chemistry.

To the best of our knowledge, TST, DFT calculations and MKM have been primarily employed in plasma catalysis modeling for ammonia synthesis [25,28], CO_2 hydrogenation [27], partial oxidation of methane [29] as well as non-oxidative coupling of methane [26]. In contrast, there has been relatively limited effort in kinetic modelling of plasma-catalytic DRM, due to the complexity of the reaction system. Pan et al. [33] developed a numerical model that couples plasma kinetics and surface kinetics to investigate the inherent mechanisms, while Zhu et al. [34] developed a 1D plasma fluid model, integrated with 0D surface kinetics, to reveal how the surface reactions on platinum catalyst influence the redistribution of gaseous species in plasma-catalytic DRM. Unfortunately, E-R interactions between

surface-adsorbed and gas-phase species were not considered in the kinetic mechanism, which might play a crucial role in plasma catalysis [7,25,27,28]. Furthermore, the rate coefficients for surface reactions were calculated using empirical formulas in the aforementioned works.

Recently, Loenders *et al.* [20] proposed a coupled plasma-surface microkinetic model. This model describes the reaction kinetics both in the plasma and on the catalyst surface simultaneously, providing insights into the effect of transition metal catalysts (i.e., Ru, Cu and Ag) on plasma-catalytic DRM. Their results revealed some interesting phenomena that the packing of transition metal catalysts in plasma-catalytic DRM may have a negative rather than positive effect on reactants conversion and products formation, due to efficient reverse reactions under typical DBD conditions dominated by radical chemistry. These finding elucidate that the different physical and chemical interactions are not only needed to optimally tailor the interplay between these effects, but also to avoid conditions under which they negatively affect the process. Finally, the authors provided important recommendations for improvement in plasma-catalytic DRM, and plasma catalysis in general. However, the model predictions could not be compared with experiments, due to the lack of data available in literature for such detailed comparison. Therefore, further investigations are needed to elucidate the underling mechanisms behind this adverse effect. Furthermore, the authors pointed out that studying these interactions separately can aid in disentangling the effects, which may be beneficial for the direct comparison of experimental results from different studies. While some works have been dedicated to plasma-catalytic DRM, the fundamental mechanisms for the kinetics enhancement by plasma-generated reactive species in surface chemistry are not yet understood. More in-depth studies are needed to clarify how plasma-excited species can interact with the catalyst surface.

Furthermore, coke deposition, which can lead to unstable plasma discharge and Ni-based catalyst deactivation, remains a significant challenge in optimizing the Ni-based catalyst for desired products in plasma-catalytic DRM [35]. This challenge may limit the use of plasma-catalytic DRM on a commercial scale. However, the underlying mechanisms for solid carbon deposition in plasma-catalytic DRM are far from understood, and the related literature is extremely limited.

Based on the above discussion, we elaborate on the effects of plasma-generated reactive species on the surface chemistry and coking kinetics in plasma-catalytic DRM in this work. For this purpose, we combine experimental measurements, catalyst characterization and chemical kinetics modeling. First, we will present our experimental data in a DBD reactor packed with and without Ni/SiO$_2$ catalyst, to demonstrate that the combination of plasma and catalyst can effectively improve the performance in DRM. Second, we will present our 0D kinetics model combined with detailed plasma-catalytic mechanism and validate it experimentally. Subsequently, we will decouple the surface kinetics from the plasma chemistry, in order to disentangle the chemical interactions into surface kinetics and plasma chemistry. We will also illustrate the results of our path flux and sensitivity analysis, to unveil the underlying promotive mechanism of the plasma-enhanced surface chemistry for products formation. Finally, we will perform the coking kinetics analysis from a chemical perspective combined with thermogravimetric analysis (TGA), which has never been explored before.

2. Experimental methods and kinetic modelling
2.1 Experimental setup

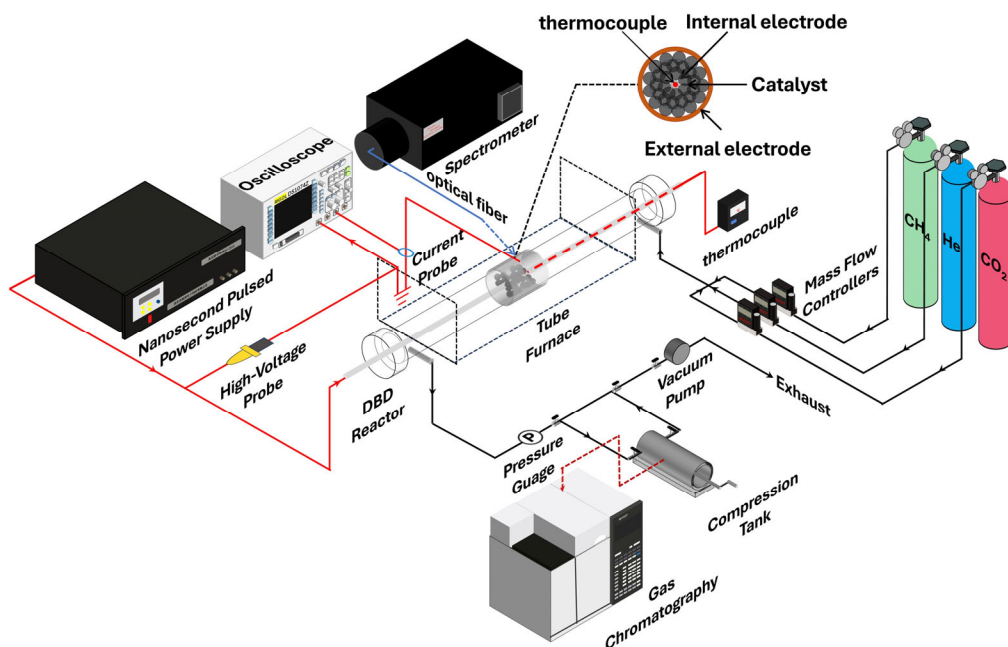**Fig. 1**. Schematic diagram of the experimental setup

As depicted in Fig. 1, we performed experiments for plasma-catalytic CH_4/CO_2 reforming in a needle-cylinder DBD reactor with 15 mm inner diameter and a barrier thickness of 2 mm. The DBD reactor consists of a quartz tube with a built-in coaxial copper electrode connected to the power supply and a concentric copper electrode with 30 mm length, attached to the outside wall of the tube, acting as the ground electrode. The diameter of the high voltage electrode was 3 mm, pre-loaded into the quartz tube with an inner diameter of 3 mm and an outer diameter of 6 mm. The discharge volume was fully packed with 1.5 g Ni/SiO_2 catalyst (see section S.1 and Fig. S1 for the preparation method in the Supporting Information (SI)). By combining H_2 temperature-programmed reduction (H_2-TPR), X-ray diffraction (XRD), and X-ray photoelectron spectroscopy (XPS) (see section S.1 and Fig. S2 in the SI) to characterize the crystallite structure, and composition of the catalyst. The characterization results reveal that the active sites of the prepared Ni/SiO_2 catalyst was in the reduced state, aligning with the proposed surface reaction mechanism (see section 2.2.2 below in detail).

The feed gas (0.15 CH_4/0.15 CO_2/0.70 He) with a total flow rate of 200 sccm, was controlled by mass flow meters (MC-1600D-PV-4W, Warwick Instruments) and mixed well before being introduced into the reactor. The purities for all gases were greater than 99.999%. In this study, the plasma was ignited using a nanosecond pulse power supply (HVP-15P, Xi'an Smart Maple Electronic Technology Co., Ltd) with a peak voltage ranging from 4000 to 8000 V, a pulse duration of 200 ns, and a repetitive frequency of 20 kHz. Although the gas mixture could be ignited at 3000 V, the conversion was relatively low, so we selected 4000 V as the initial applied voltage in this study. A tube furnace (Tianjin Zhonghuan Furnace Crop.) was used to control the reaction temperature at a constant value (50-250 ℃ at steps of 50 ℃). It is worth noting that the temperature could not be maintained at room temperature due to the absence of circulating water as the ground electrode, so we chose 50 ℃ as the starting point. To highlight the advantages of NTP, we selected a mild temperature range of 50-250 ℃. At the same time, a type-K thermocouple probe (± 1 K) was located at the end of the discharge region to measure the temperature. The pressure was controlled by a vacuum pump and needle valve to maintain a constant value in the range of 8-40 kPa at intervals of 8 kPa. To address the complexity of the 0D model in this work, we adopted reduced pressure, highly diluted CH_4/CO_2 mixture and a nanosecond pulsed power supply to make the discharge in packed bed DBDs more uniform [7,36] compared to the filamentary behavior observed in AC discharges [3,35]. Additionally, the extremely short duration of each pulse

results in nanosecond-scale heating of the discharge channels, thereby leading to relatively low gas temperature in nanosecond pulsed discharges, which is beneficial for controlling the reaction temperature. Furthermore, the nanosecond pulsed discharge is characterized by short durations and microsecond-scale afterglow periods (reduced electric field = 0 Td), which simplifies the discharge physical model. All electric characteristics were recorded by a digital oscilloscope (RIGOL DS1104Z, 100 MHz, 1GSa/s) equipped with a high voltage probe (RIGOL RP1018H, 1000:1) and a current probe (CYBERTEK CP8030B, 100:1). The optical emission spectroscopy (OES) diagnostics of the plasma were conducted using an optical fiber connected to an Acton spectrometer (SP-2500i, 1200 g/mm grating, Princeton Instrument) with a focal length of 500 mm to record the spectra during the DRM reaction. Gas samples collected by a sample vessel were analyzed off-line using an Agilent 7890B gas chromatograph (GC) equipped with a flame ionization detector (FID) and a thermal conductivity detector (TCD). Each measurement was repeated three times to ensure that the measurement error was less than 5.0%. In this study, the products of plasma-catalytic DRM were dominated by syngas, so the gas expanded upon reaction. Thus, we corrected the concentration of products based on the method explained in Ref [37] to compensate for the influence of the volume change on the conversion and selectivity. The calculation method for reactant conversion, product selectivity, and yield can be found in the SI, section S.2.

2.2 Kinetic model

We developed a 0D plasma catalysis kinetics model to elucidate the effects of plasma-generated reactive species on the surface chemistry and coking kinetics in nanosecond-pulsed DBD plasma-catalytic DRM. We used a hybrid ZDPlasKin-CHEMKIN model [38], incorporating the plasma kinetics solver ZDPlasKin [23] and the chemical kinetics solver CHEMKIN-II [39], to predict the time evolution of species densities using a time-splitting method, resulting in the decoupling of plasma kinetics from low temperature chemistry. The rate coefficients of electron impact reactions were computed by the Boltzmann equation solver BOLSIG+ [40], which is incorporated into ZDPlasKin. The reduced electric field (E/N) was determined by the power density and calculated at each time step [41].

Table 1 Species considered in the model of plasma-catalytic CH_4/CO_2 reforming

Species Type	Symbol	Number
Molecules	H_2, O_2, O_3, H_2O, H_2O_2, He, CO, CO_2, CH_4, CH_2O, CH_3OH, HCOOH, CH_2CO, CH_3O_2H, C_2, C_2H_2, C_2H_4, C_2H_6, CH_3CHO, C_2H_5OH, aC_3H_4, cC_3H_4, pC_3H_4, C_3H_6, C_3H_8	25
Atoms/Radicals	H, O, C, OH, HO_2, CH, CH_2, $CH_2(S)$, CH_3, HCO, CH_3O, CH_2OH, CHOH, COOH, HCOO, CH_3O_2, C_2H, H_2CC, C_2H_3, C_2H_5, C_2O, HCCO, CH_3CO, CH_2CHO, C_2H_5O, CH_2CH_2OH, CH_3CHOH, CH_2CHOH, C_3H_2, C_3H_3, aC_3H_5, sC_3H_5, tC_3H_5, iC_3H_7, nC_3H_7	35
Vibrationally excited species	H_2(v1), H_2(v2), H_2(v3), H_2O(v010), H_2O(v001), H_2O(v001), CH_4(v24), CH_4(v13), CO_2(va), CO_2(vb), CO_2(vc), CO_2(vd), CO_2(v1)-CO_2(v9), CO(v1)-CO(v10)	31
Electronically excited species	$He(2^3S)$, $O(^1D)$, $O(^1S)$	3
Cations	He^+, H^+, H_2^+, H_3^+, O^+, O_2^+, OH^+, H_2O^+, H_3O^+, CO^+, CO_2^+, C^+, CH^+, CH_2^+, CH_3^+, CH_4^+, CH_5^+, C_2^+, C_2H^+, $C_2H_2^+$, $C_2H_3^+$, $C_2H_4^+$, $C_2H_5^+$, $C_2H_6^+$	24
Anions	e, H^-, O^-, O_2^-, OH^-	5
Surface-adsorbed species	H(s), O(s), OH(s), H_2O(s), C(s), CH(s), CH_2(s), CH_3(s), CO(s), HCO(s), COH(s), CHOH(s), CH_2O(s), CH_2OH(s), CH_3O(s), COOH(s), HCOO(s), CH_3OH(s), HCOOH(s), C_2H_2(s), C_2H_4(s), Ni(s)	22
Solid Carbon	C_{soot} [42]	1

Note: $CH_2(S)$ is an isomer of the CH_2 radical; CO_2(v9) is the sum of higher vibrational states; X(s) indicates the surface-adsorbed species.

2.2.1 Plasma-kinetic mechanism

The detailed plasma-kinetic mechanism consists of neutral molecules, radicals, vibrationally and electronically excited species, ions and surface-adsorbed species, as listed in Table 1. The gas-phase chemistry set was primarily built upon our previous works, known for its excellent prediction ability [43-45]. Some reactions from the NIST Chemical Kinetics Database were integrated into the chemistry set [46], resulting in total in 624 chemical reactions (see SI, chemkin.inp). Only 9 asymmetric vibrational mode levels ($CO_2(v1)$-$CO_2(v9)$) and 4 effective levels of the symmetric vibrational modes ($CO_2(va)$-$CO_2(vd)$) were considered, with $CO_2(v9)$ being the sum of the higher vibrational states [47], along with their corresponding cross-sections [48]. This is more than sufficient for DBD plasma [49]. Regarding the electron impact dissociation of CO_2, three channels $e + CO_2 \rightarrow e + CO + O$, $e + CO_2 \rightarrow e + CO + O(^1D)$ and $e + CO_2 \rightarrow e + CO + O(^1S)$ were considered [50]. Noxon [51] and Slanger *et al.* [52] experimentally demonstrated that the dissociation of CO_2 can result in the production of $O(^1D)$ and $O(^1S)$. Most of the cross-sections for electron impact reactions are available from our previous works [35,45,53].

We took into account in detail the vibrational kinetics, including vibrational energy exchange reactions and chemical reactions stimulated by vibrational states. Three main types of vibrational relaxation reactions, i.e., vibrational-translational (V-T) transitions, vibrational-vibrational (V-V) exchange among two modes or among two molecules in the same mode were considered. The rate constants of chain branching reactions accelerated by vibrationally excited molecules were defined by the Fridman-Macheret α-model [54]. This is an approximation, but at this stage, no better model is available. Moreover, the vibrational kinetics have very limited contribution to the gas phase chemistry, as we will demonstrate later, so the effect of this approximation is minimal. A detailed chemistry set involving $O(^1D)$ and $O(^1S)$ was incorporated to describe the electronic kinetics [35,43]. Furthermore, we incorporated the ion-neutral, electron-ion recombination and mutual neutralization reactions into the ion chemistry mechanism. In summary, 124 species (see Table 1, including the phase change of carbon, i.e., deposition of C_{soot}, which is included as part of the plasma chemistry) and 1833 elementary reactions (see SI, plasma_kinetics.inp) were included in the plasma kinetic mechanism.

2.2.2 Plasma-surface interactions

In this section, we considered not only the traditional adsorption, Langmuir-Hinshelwood (L-H) and desorption reactions, but also the direct adsorption of radicals on the catalyst surface, the dissociative adsorption of vibrationally excited molecules, and E-R interactions.

Given an elementary reaction step, $A + B \rightarrow AB^\# \rightarrow C + D$, with a transition state (TS) species $AB^\#$ for example, the forward rate coefficient k_f can be expressed based on the harmonic TST [25,27],

$$k_f = \frac{k_B T}{h} \exp\left(-\frac{\Delta H^\#}{RT}\right) \exp\left(\frac{\Delta S^\#}{R}\right) \tag{1}$$

where k_B is the Boltzmann constant, h is the Planck constant, R is the universal gas constant, $\Delta H^\#$ and $\Delta S^\#$ are the activation enthalpy and entropy barriers for the reaction step, respectively.

Accordingly, the backward rate coefficient k_r can be derived from the equilibrium constant K_{eq},

$$\frac{k_f}{k_r} = K_{eq} = \exp\left(-\frac{\Delta H^r}{RT}\right) \exp\left(\frac{\Delta S^r}{R}\right) \tag{2}$$

where ΔH^r and ΔS^r are the reaction enthalpy and entropy for the reaction step, respectively.

In this section, the data for L-H, molecule adsorption and desorption mechanisms were derived from DFT calculations [55]. Given the weak physisorption of CH_4 and CO_2 with a low adsorption energy of -0.02 eV [56,57], their adsorption and dissociation on Ni catalyst surface can be effectively combined into one step for each molecule: $CH_4 + 2Ni(s) \rightarrow CH_3(s) + H(s)$ and $CO_2 + 2Ni(s) \rightarrow CO(s) + O(s)$ [57]. The combination of two chemisorbed H to $H_2(s)$ and the desorption of $H_2(s)$ were also represented in one step for the same reason.

Direct chemical adsorption of radicals is strongly exothermic. We assume it can happen quickly without an enthalpy barrier and the rate constants for radical adsorption assume the complete loss of translational entropy associated with moving from the gas phase to the adsorbed state [25,27,28], simplified as follows:

$$k_{ads} = \frac{k_B T}{h} \exp\left(\frac{\Delta S^{\#}}{R}\right) \tag{3}$$

Further, plasma-induced vibrational excitation can elevate the enthalpy of reactant molecules, thereby lowering the activation barrier for their dissociation on the catalyst surface. The rate coefficient for plasma-enhanced dissociative adsorption is assumed to follow an α model [30]:

$$k_{ads,v} = \frac{k_B T}{h} \exp\left(\frac{\Delta S^{\#}}{R}\right) \exp\left(-\frac{\Delta H^{\#} - \alpha E_v}{RT}\right) \tag{4}$$

here, E_v represents the energy for a reactant in the vth vibrational level, and α is the efficiency factor to describe the utilization of the vibrational energy to lower the dissociative adsorption barrier. The α model is only a rough approximation to account for the dissociative adsorption enhanced by vibrationally excited molecules, which has to be kept in mind when analyzing the results. However, to date, no exact expressions for the efficiency of utilizing the vibrational energy to lower the dissociative adsorption barrier have been determined in plasma catalysis.

In contrast to thermal catalysis, the E-R reactions are potentially important in plasma-catalytic processes due to the elevated radical concentrations. E-R reactions involving free radicals do not require the breaking of initial chemical bonds before the formation of adsorbate-adsorbate bonds. Consequently, E-R reactions are considered to be enthalpy barrierless and limited by entropy loss going from a gas phase state to a surface state [25,27,28]. Furthermore, T.W. Liu $et\ al.$ [58] comprehensively examined the energetics of 51 reactions on various metal surface via DFT, finding that enthalpic barriers for E-R reactions involving N and H radicals were negligible, thereby providing substantial support for this assumption. The rate coefficients for E-R interactions are calculated using Eq. (5)

$$k_{ER} = \frac{k_B T}{h} \exp\left(\frac{\Delta S^{\#}}{R}\right) \tag{5}$$

It is worth to mention that rate coefficients calculated using Eq. (5) for E-R reactions may overestimate the rates of some reactions, introducing uncertainties in our results. Unfortunately, obtaining accurate parameters from experimental fits or DFT/AIMD simulations to determine E-R reaction rate coefficients is often difficult or computationally very expensive. To address this challenge, we performed a sensitivity analysis where we varied the rate coefficients to evaluate the importance of E-R reactions in this work.

Additionally, we considered E-R reactions involving gas-phase molecules like CO_2 (CO_2 + H(s) → COOH(s), CO_2 + H(s) → HCOO(s)) and CO (CO + H(s) → HCO(s), CO + H(s) → COH(s)). Contrary to E-R reactions involving radicals, these reactions have enthalpy barriers, like the E-R reactions involving CH_4 considered by Loenders $et\ al$ [29]. The activation barriers were estimated based on the potential energy surfaces of the corresponding L-H reactions involving CO_2(s) and CO(s), along with the desorption energy of CO_2(s) and CO(s). Consequently, vibrationally excited molecules can stimulate the E-R reactions, and we calculated the rate coefficients using the same α model mentioned above, keeping in mind it is only an approximation, but no better estimation is available in literature. In all cases, the surface temperature was assumed to be equal to the gas temperature. This is reasonable because the characteristics of nanosecond pulsed discharge and the endothermic nature of the DRM reaction result in a much lower temperature rise during discharge, and the long afterglow periods between pulses allow for effective heat transfer between the gas and surface, leading to temperature equilibrium. Additionally, the temperature measured by thermocouple probe and tube furnace are almost the same in this study. The proposed plasma-enhanced catalytic

mechanism includes 22 adsorbed species (see Table 1) and 219 surface reaction steps (see SI, chemkin.inp).

2.2.3 Entropy values

The activation entropy is calculated as the difference in entropy between TS and initial state (IS), while the reaction entropy is calculated as the difference in entropy between final state (FS) and IS. For adsorbates tightly bound on the surface, the entropy of these species is assumed equal to zero, since they have lost most of their translational and rotational modes [27]. However, the TS for reactions involving gas phase species is commonly treated as a two-dimensional (2D) ideal gas in the xy plane and as a harmonic oscillator in the z direction. In this case, only one degree of translational motion is replaced by one vibrational mode in z. Thus, the entropy for the TS can be written as

$$S_{TS}(T) = S_{gas}^0 - \frac{1}{3} S_{gas,trans}^0 + S_{ad,vib,z}^0 \tag{6}$$

They exhibit a nearly negligible contribution to the vibrational entropy due to a very restricted center-of-mass motion in z [59,60]. The value for S_{trans} can be calculated using the Sackur-Tetrode equation.

$$S_{trans}(T) = R \ln \left(\frac{\left(2\pi m k_B T / h^2 \right)^{3/2} e^{5/2}}{\left(N_A / V_{gas}^0 \right)} \right) \tag{7}$$

$$S_{gas,trans}^0 = S_{Ar,298K}^0 + R \ln \left[\left(m / m_{Ar} \right)^{3/2} \left(T / 298K \right)^{5/2} \right] \tag{8}$$

where, m and m_{Ar} are the molar mass of the gas and argon, respectively, N_A is the Avogadro constant, V_{gas}^0 is the molar volume of the gas at its standard state, and $S_{Ar,298K}^0$ is the entropy of Ar at 298 K and 1 atm.

It is worth noting that dissociative adsorption is an exception: we assumed that the TS is tightly located at the surface, resulting in zero entropy. This assumption is based on the strong interaction with the catalyst, which is necessary for dissociation.

## 3. Results and discussion

3.1 Model validation

We performed steady-state measurements of the products and reactants to investigate the enhancing effects of the combination of Ni/SiO$_2$ catalyst with nanosecond-pulsed discharge-activated DBD plasma on DRM. Fig. 2 presents a comparison between the experimental and simulation results for CH$_4$ and CO$_2$ conversion under varying conditions of applied voltage (a) and temperature (b), at a discharge frequency of 20 kHz and total gas pressure of 16 kPa. As depicted in Fig. 2(a), there is a clear upward trend in conversion from 9% to 20% and from 3% to 11% for CH$_4$ and CO$_2$, respectively, attributed to more energy deposited into the discharge mixture with increasing voltage. Fig. 2(b) illustrates that the conversion increases from 9% to 17% for CH$_4$ and from 5% to 11% for CO$_2$ upon rising temperature, owing to the enhancement of the reduced electric field E/N with increasing temperature. It is worth noting the highest total conversion of 16% was achieved at 8000 V and 473 K (see Fig. S3 in the SI). The calculated conversions are in excellent agreement with the measured data, both in absolute values and in trends as a function of applied voltage and temperature. To highlight the promotive effect of combining plasma and catalyst on the reforming of CH$_4$ and CO$_2$, we also performed experiments for an unpacked DBD plasma and for thermo-catalytic reforming. No conversion was detected for the thermo-catalytic CH$_4$/CO$_2$ reforming, and in the unpacked DBD, the conversions were significantly lower (see Fig. 2, empty bars), illustrating the enhancement in the plasma catalysis system.
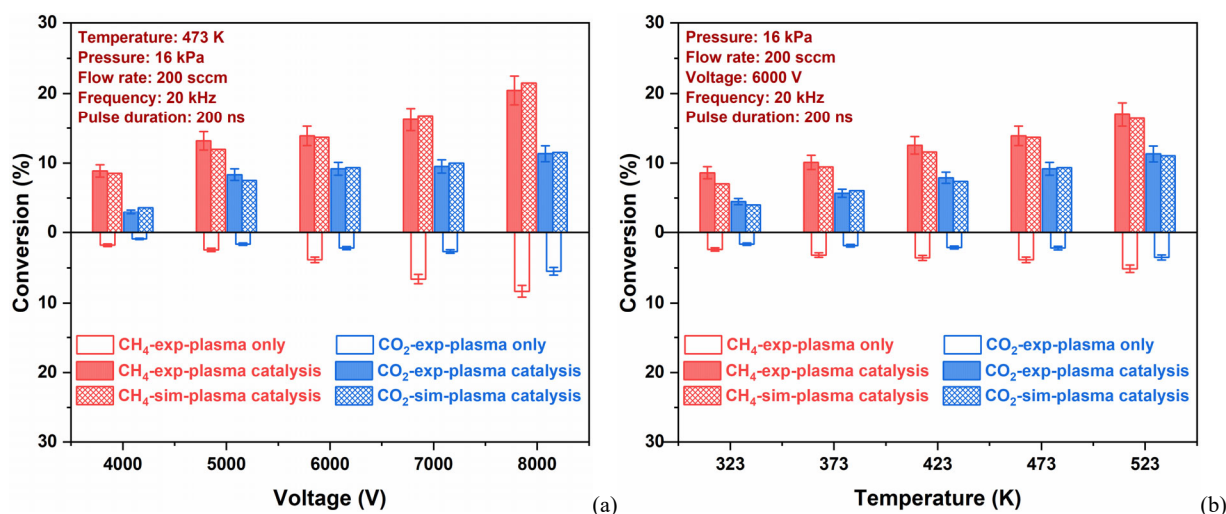
Fig. 2. Comparison of CH_4 and CO_2 conversion between experimental measurements and model predictions as a function of (a) applied voltage and (b) reaction temperature in plasma-catalytic reforming of CH_4 and CO_2. (exp: experiments; sim: simulation)

Fig. 3 shows the comparison between steady-state measurements and model predictions for product selectivity at the same conditions as in Fig. 2. The experiments indicate that the primary products include syngas (CO/H_2) and ethane (C_2H_6). CO and H_2 reach the highest selectivity of 78% and 75%, respectively, at a voltage of 8000 V and temperature of 473 K. The corresponding CO and H_2 yields are 15% and 12%, respectively (see Fig. S4 in the SI). Regarding the formation of minor species, several hundred ppm of C_2H_2, C_2H_4 and C_3H_8 were detected in the experiments. Due to the absence of a cooling trap [3,35] to condense the liquid products before the samples were injected into the column from the reactor's outlet, the oxygenates were characterized employing a DB-WAX GC column (123-7032, 30 m × 0.320 mm). Due to the characteristics of the DB-WAX GC column, only formaldehyde and methanol could be detected. A maximum selectivity of 11% for total oxygenates was achieved in the experiments at 4000 V and 473 K, while the highest oxygenates yield of 0.9% was obtained at 5000 V and 473 K (see Fig. S4 in the SI). We can conclude that lower voltage and temperature are beneficial for the formation of oxygenates, which is consistent with our previous work [35]. Notably, the selectivity for syngas increases with increasing voltage and temperature, whereas the selectivity for hydrocarbons and oxygenates decreases with increasing voltage and temperature. From a thermodynamic perspective, as conversion increases, the equilibrium for DRM shifts toward the final products (CO, H_2), resulting in decreased selectivity for hydrocarbons and oxygenates. At the same time, the analysis of the chemical reaction mechanism also confirms this conclusion (see section S.5 in the SI). Moreover, to illustrate the enhancing effect of plasma catalysis on the product selectivity, we compare with plasma-only. Evidently, plasma catalysis can enhance the selectivity towards syngas and oxygenates, highlighting the promotive effect of combined Ni/SiO_2 catalyst and plasma on reforming of CH_4 and CO_2.
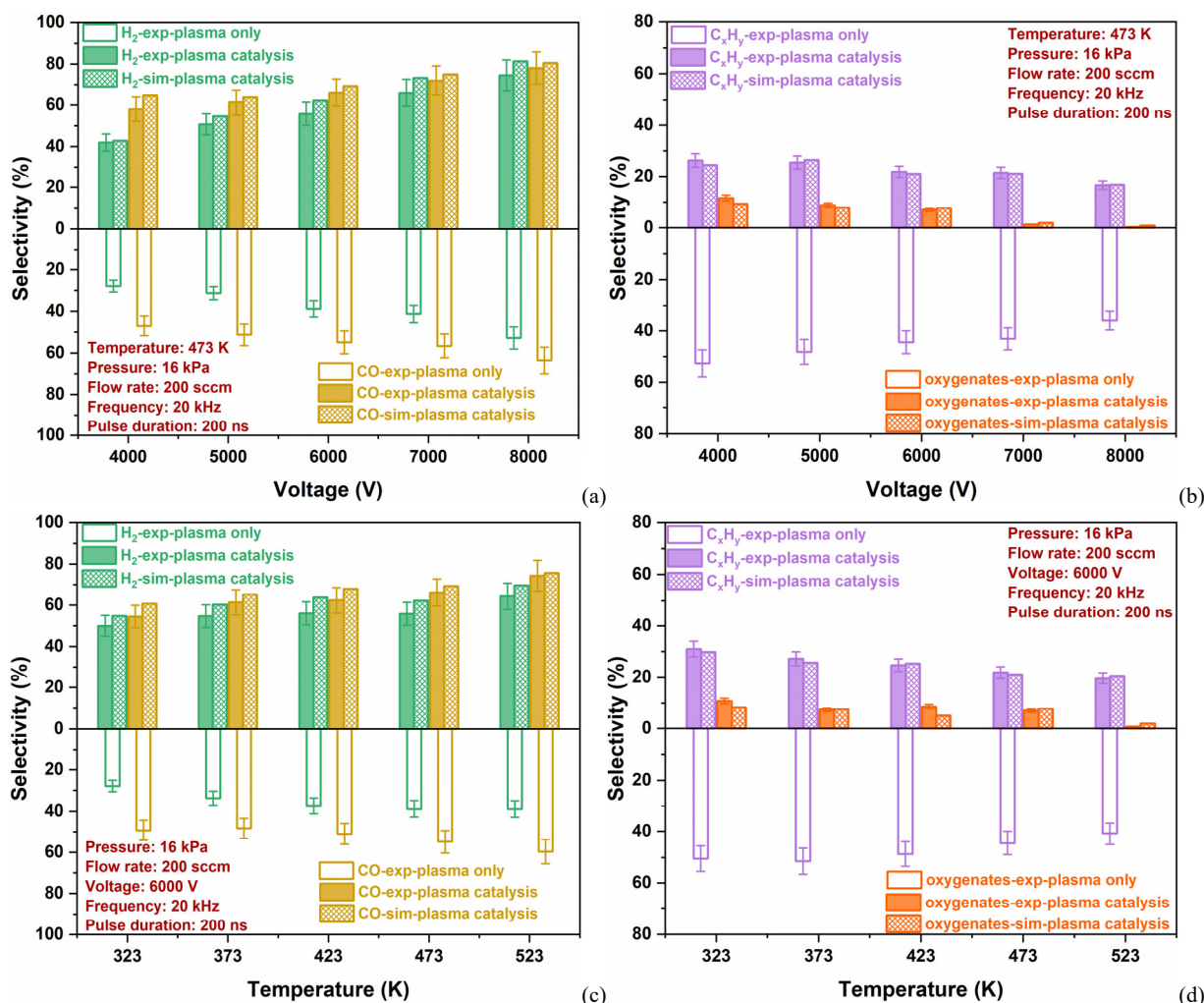
Fig. 3. Comparison of the products selectivity between experimental measurements and model predictions as a function of applied voltage: (a) syngas; (b) hydrocarbons and oxygenates. Comparison of the products selectivity between experimental measurements and model predictions as a function of reaction temperature: (c) syngas; (d) hydrocarbons and oxygenates. (exp: experiments; sim: simulation; C_xH_y indicates the sum of all hydrocarbons)

As mentioned above, we compared the predicted reactants conversion and products selectivity with the experimental measurements to validate our kinetic model. As depicted in Figs. 2-3, the model predictions agree well with the steady-state measurements, with a relative deviation less than 10% for most species. Additionally, emission spectra were recorded to characterize the reactive intermediates formed during the plasma-assisted DRM process. Fig. S5 in the SI shows a typical emission spectrum measurement of a 0.70 He/0.15 CH_4/0.15 CO_2 plasma with and without packing of Ni/SiO_2 catalyst. The detailed emission lines of the main species detected are listed in Table S1. H_α, O, and He atomic lines, and CO_2, CO_2^+, CO, CO^+, CH, and C_2 bands were identified, confirming the presence of a variety of reactive intermediates, such as H, O, CO_2^+, CO, CO^+, CH, and C_2. In summary, the steady-state measurements and OES characterization indicate that our detailed kinetic model can present a realistic picture of the underlying chemical mechanisms. Motivated by the aim of this work, we will conduct a kinetic analysis based on the simulation results. The experimental condition at 473 K and 6000 V, which enables the simultaneous generation of syngas, hydrocarbons, and oxygenates, while effectively incorporating the specific investigated temperature and voltage points, was selected for analysis.

3.2 Kinetics of excited species and adsorbed species
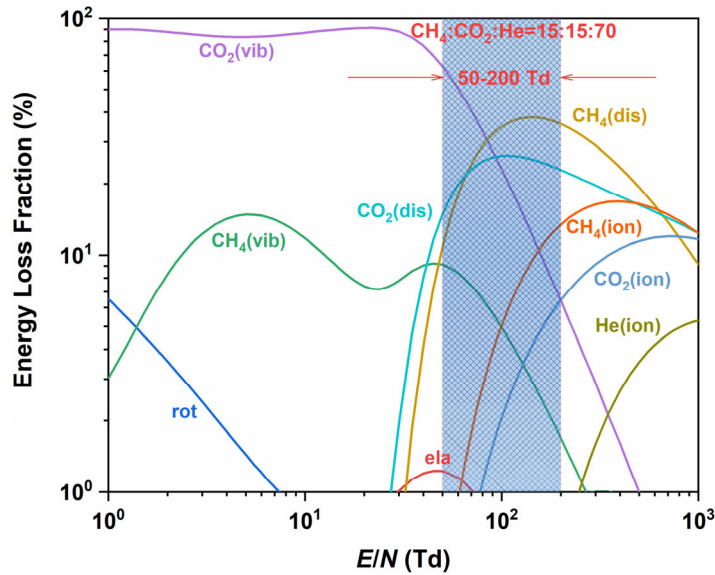
Fig. 4. Fraction of plasma energy deposited into different excitation modes in a 0.15 CH_4/0.15 CO_2/0.70 He mixture as a function of E/N. (ela: elastic; rot: rotational excitation; vib: vibrational excitation; dis: dissociation; ion: ionization)

The reduced electric field, E/N, is one of the most crucial parameters in controlling the distribution of electron energy deposition to various excitation modes and the formation of active species in a non-equilibrium plasma. Fig. 4 shows the fraction of electron energy deposited into different excitation channels as a function of E/N for a 0.15 CH_4/0.15 CO_2/0.70 He mixture. The blue region indicates the range of E/N values for the discharge conditions described in our kinetics model. As shown in Fig. 4, the most efficient mechanism for electron energy loss is the vibrational excitation of CO_2 and CH_4 at a relatively low reduced electric field (< 50 Td), facilitating the dissociative adsorption of reactant molecules on the surface. In our studied E/N range (50 Td ~ 200 Td), the electron energy is primarily transferred to the dissociation and ionization modes of CH_4 and CO_2, as well as the CO_2 vibrational excitation channel, which benefits the surface reactions via direct adsorption of radicals and E-R reactions.
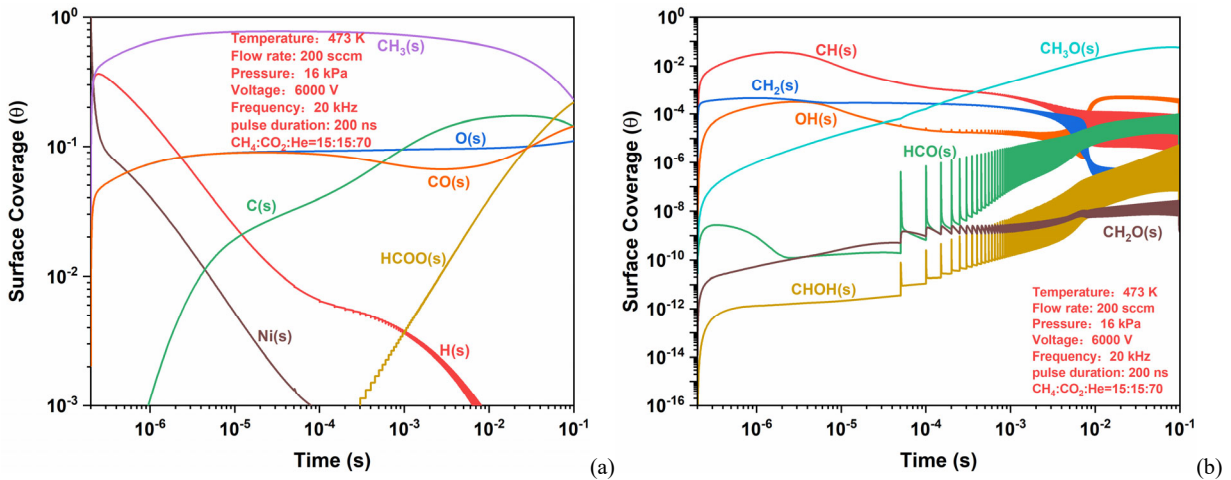
Fig. 5. Time-dependent evolution of surface coverage for (a) the main adsorbed species and (b) the minor adsorbed species (CH_4:CO_2:He = 15:15:70; flow rate: 200 sccm; pressure: 16 kPa; reaction temperature: 473 K; applied voltage: 6000 V; discharge frequency: 20 kHz; pulse duration: 200 ns).

Fig. 5 shows the time-dependent evolution of the surface coverage for the primary adsorbed species in plasma-catalytic CH_4/CO_2 reforming. As seen in Fig. 5(a), the rapidly increasing surface coverages of $CH_3(s)$, $H(s)$, $CO(s)$ and $O(s)$ result in a sharp drop in the density of free sites ($Ni(s)$) in the early afterglow stage of the first pulse. This is mainly because the reactions on the catalyst surface are dominated by the dissociative adsorption of CH_4 and CO_2, resulting in the catalyst surface being almost fully covered with adsorbed species. A lower CH_4 activation energy on the Ni surface leads to dominant $CH_3(s)$ and $H(s)$ coverages over $CO(s)$ and $O(s)$. The surface coverage of $H(s)$ shows a decreasing trend due to the recombination reaction $H(s) + H(s) \rightarrow H_2 + 2Ni(s)$, yielding the production of H_2. After about 0.3 ms, the vibrationally excited $CO_2(v)$ take part in E-R reactions with $H(s)$: $CO_2(v) + H(s) \rightarrow HCOO(s)$, leading to a sharp increase in the surface coverage of $HCOO(s)$. The surface coverage of $CO(s)$ gradually increases at a later stage of the process, as $HCO(s)$ undergoes dehydrogenation: $HCO(s) + Ni(s) \rightarrow CO(s) + H(s)$ on the free sites on the catalyst surface.

As observed from Fig. 5(b), the surface coverage of $CH(s)$, $CH_2(s)$ and $OH(s)$ is higher in the afterglow stage of the first pulse. $CH_2(s)$ and $CH(s)$ are formed via stepwise dehydrogenation of $CH_3(s)$ on the catalyst surface (see Fig. 10 below in detail). $OH(s)$ is primarily generated through the L-H reaction: $CH(s) + O(s) \rightarrow C(s) + OH(s)$ during this period, resulting in a higher coverage. In the final stage, high concentrations of reactive H atoms lead to the rapid formation of $OH(s)$ through the E-R hydrogenation reaction: $O(s) + H \rightarrow OH(s)$. The increased coverage of $OH(s)$ accelerates the primary $CH_2(s)$ consumption reaction: $CH_2(s) + OH(s) \rightarrow CH_3(s) + O(s)$, resulting in a rapid decrease in the $CH_2(s)$ coverage.

$CH_3O(s)$ is primarily formed through the oxidation reaction: $CH_3(s) + O \rightarrow CH_3O(s)$, resulting in a rapid increase in the $CH_3O(s)$ coverage. With the gradual formation of CO in the gas phase, the vibrational excitation of CO becomes important. Consequently, the generated vibrational states $CO(v)$ further enhance the $HCO(s)$ formation via the E-R reaction: $CO(v) + H(s) \rightarrow HCO(s)$. Additionally, the hydrogenation of $HCO(s)$ through the E-R process: $HCO(s) + H \rightarrow CH_2O(s)$, is also accelerated, facilitating the generation of $CH_2O(s)$. Therefore, the coverage of $HCO(s)$ and $CH_2O(s)$ increases rapidly with increasing reaction time and exhibits a periodical tendency. $CHOH(s)$ is mostly generated through the hydrogeneration reaction: $COH(s) + H \rightarrow CHOH(s)$. Thus, the coverage of $CHOH(s)$ increases upon increased $COH(s)$ coverage. It is worth noting that the adsorbed species were not detected in this work due to the absence of an *in situ* characterization technique. However, Kosari *et al.* [61] and Shi *et al.* [62] have identified several surface species, such as $CO(s)$, $OH(s)$, $CH_3(s)$, $HCOO(s)$, $HCO(s)$ on the Ni/SiO_2 catalyst surface in DRM process using *in situ* DRIFTS, providing additional validation for the simulation results.

3.3 Enhancement effect of plasma species on surface reactions

As mentioned above, vibrationally excited species or plasma radicals may facilitate certain reactions at the catalyst surface, allowing catalysts to perform better in the overall catalytic process. In this section, we will demonstrate the importance of surface reactions involving plasma species by comparing their rate coefficients and reaction rates with those of surface dissociation and L-H steps, which dominate in thermal catalysis.
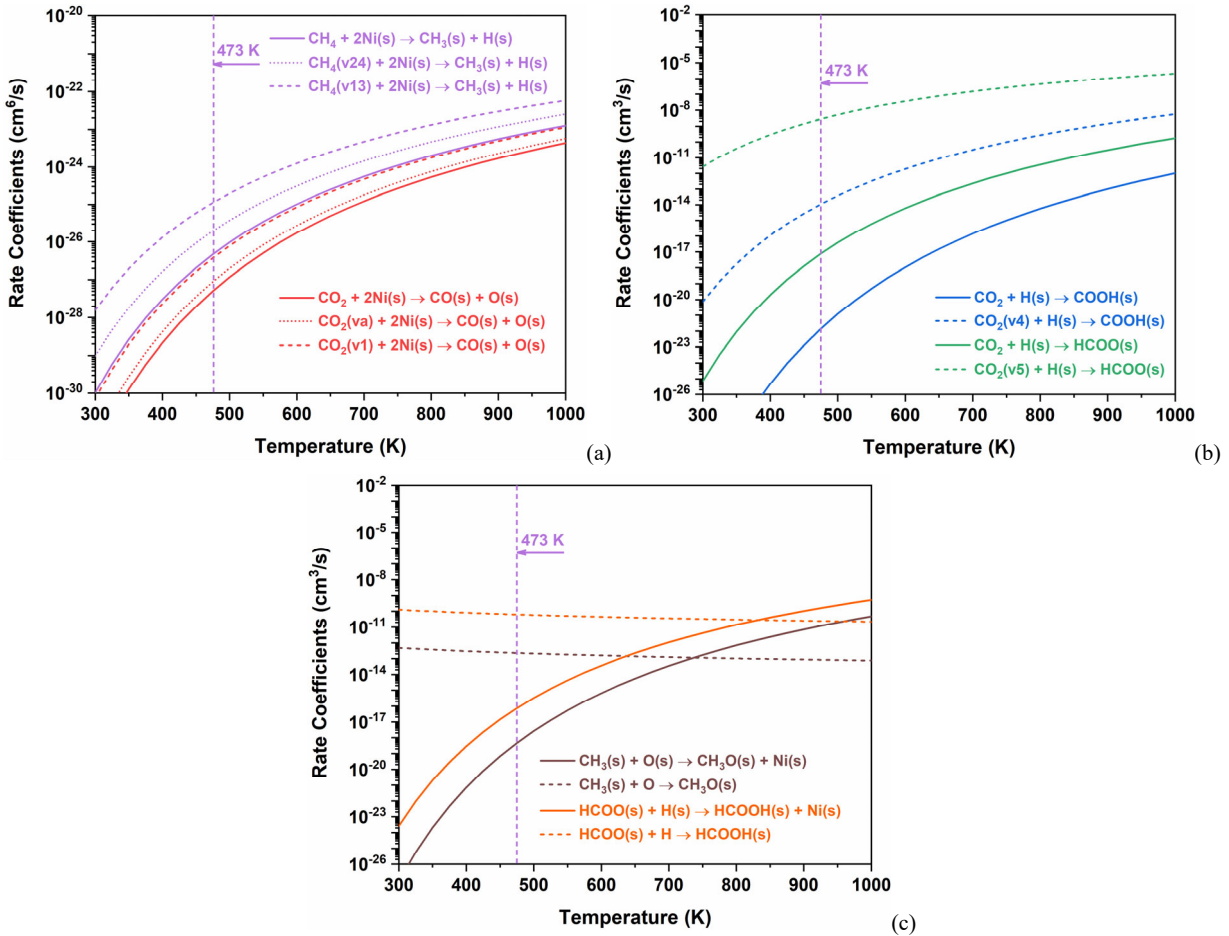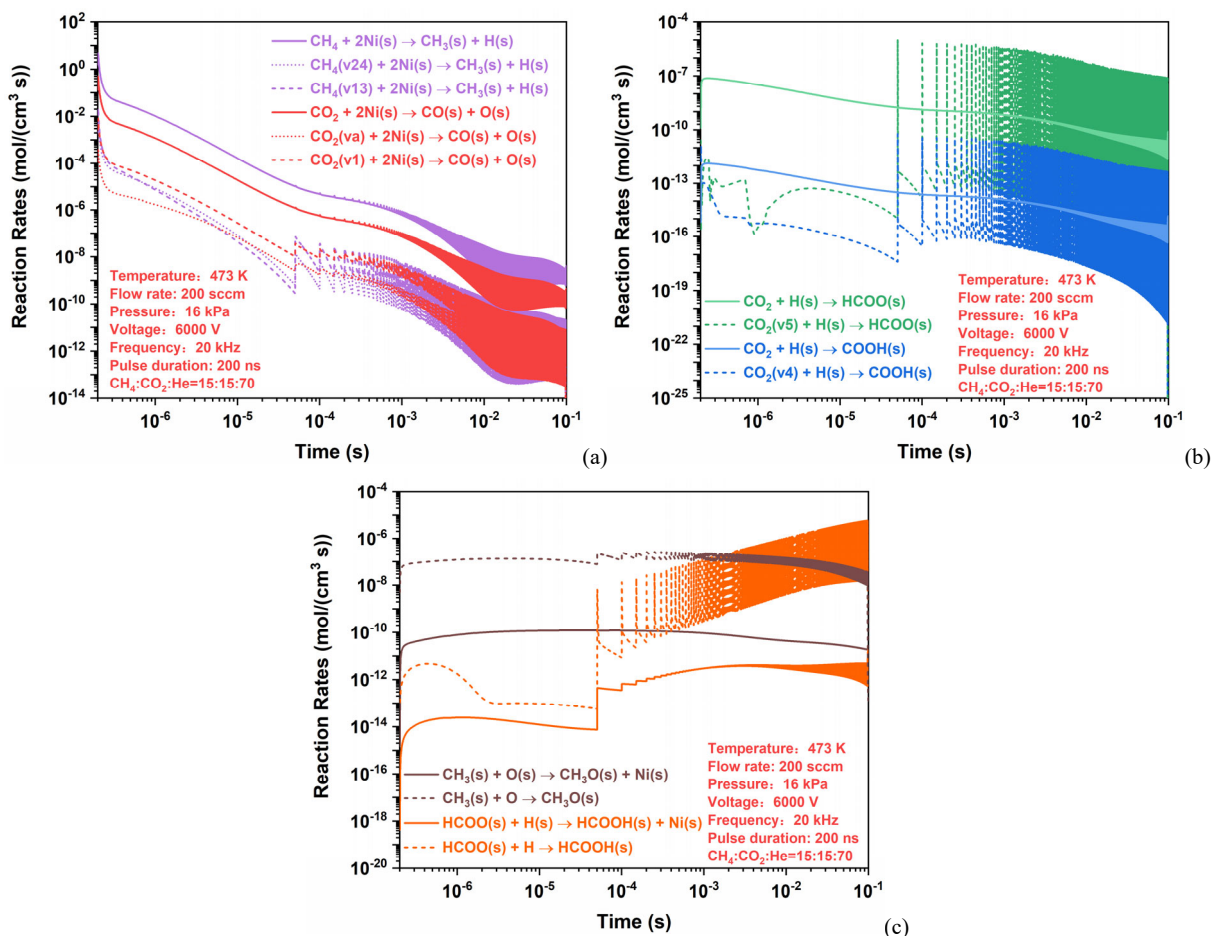
Fig. 6. Rate coefficients as a function of temperature for (a) dissociative adsorption and (b) E-R reactions from the ground state and stimulated by vibrational excitation, and (c) E-R and corresponding L-H reactions. The temperature of 473 K is characteristic for our DBD experiments.

In order to evaluate the effect of plasma-induced vibrational excitation on the catalyst surface chemistry, we plot in Fig. 6 the rate coefficients as a function of temperature of various dissociative adsorption reactions (a), and of E-R reactions (b) from ground state CO_2 and CH_4, as well as from the vibrationally excited molecules. As shown in Fig. 6(a), the rate coefficients for dissociative adsorption of vibrational states $CH_4(v)$ and $CO_2(v)$ are higher than those for ground-state CH_4 and CO_2, by 1~2 orders of magnitude. The rate coefficients for surface dissociation increase with increasing vibrational energy levels. In addition, from Fig. 6(b), it is evident that vibrationally excited $CO_2(v)$ can accelerates the E-R processes, $CO_2 + H(s) \rightarrow COOH(s)$ and $CO_2 + H(s) \rightarrow HCOO(s)$ as well.

In addition, in Fig. 6(c), we compare the rate coefficients of some E-R reactions with the corresponding L-H reactions as a function of temperature. Since the entropy value of the species increases with temperature, the rate coefficients for E-R reactions exhibit a monotonically decreasing trend with increasing temperature, while the L-H reactions behave in the opposite manner. It is clear that the rate coefficients for E-R reactions are significantly higher than those for L-H reactions in the low-temperature range. Therefore, it is easy to overcome the thermodynamic disadvantages of DRM, facilitating the catalytic activation and conversion of CH_4 and CO_2 at low temperatures.

Fig. 7. Time evolution of reaction rates of (a) dissociative adsorption and (b) E-R reactions from the ground state and stimulated by vibrational excitation, and (c) E-R and corresponding L-H reactions (CH_4:CO_2:He = 15:15:70; flow rate: 200 sccm; pressure: 16 kPa; reaction temperature: 473 K; applied voltage: 6000 V; discharge frequency: 20 kHz; pulse duration: 200 ns).

As shown in Fig. 7(a), the reaction rates of dissociative adsorption of ground state molecules CH_4 and CO_2, as well as vibrationally excited $CH_4(v)$ and $CO_2(v)$ decrease as a function of time, which is due to the decreasing surface sites density. Fig. 7(a) shows that the rates of the reactions $CH_4 + 2Ni(s) \rightarrow CH_3(s) + H(s)$ and $CO_2 + 2Ni(s) \rightarrow CO(s) + O(s)$ are 1~2 orders of magnitude higher than those of the corresponding reactions involving vibrationally excited molecules. This results from the combination of the higher ground state densities (3 orders of magnitude higher) vs lower rate coefficients (1~2 orders of magnitude lower, cf Fig. 6(a)).

In Fig. 7(b), the reaction rates for E-R reactions involving vibrationally excited $CO_2(v)$ are several orders of magnitude higher than those of the corresponding E-R reactions involving ground-state CO_2. Note that this is true during the pulses and early afterglow stages, because the vibrationally excited $CO_2(v)$ rise rapidly in the pulses, while they are lower in the later afterglow stages. However, overall they are higher, as follows also from our later (path flux) analysis (see below). This indicates that vibrationally excited $CO_2(v)$ can also significantly accelerate the E-R reactions, facilitating the formation of $COOH(s)$ and $HCOO(s)$, and further promoting the generation of $CO(s)$ and $HCOOH(s)$ through the L-H reaction $COOH(s) + Ni(s) \rightarrow CO(s) + OH(s)$, and E-R reaction $HCOO(s) + H \rightarrow HCOOH(s)$, respectively.

Furthermore, Fig. 7(c) shows that the reaction rates of plasma-enhanced E-R reactions $CH_3(s) + O \rightarrow CH_3O(s)$ and $HCOO(s) + H \rightarrow HCOOH(s)$ are approximately three and four orders of magnitude higher than those of the corresponding L-H reactions $CH_3(s) + O(s) \rightarrow CH_3O(s) + Ni(s)$ and $HCOO(s) + H(s) \rightarrow HCOOH(s) + Ni(s)$,

respectively, underscoring the high reactivity for E-R reactions involving radicals in plasma catalysis, effectively promoting and altering the surface reaction pathways. Note however, that our model may also overestimate the importance of E-R reactions, as it assumes that the E-R reaction rate coefficients are calculated using a 0 eV enthalpy barrier, and this assumption is subject to some uncertainties. Michiels *et al.* [63] proposed introducing a sticking coefficient that accounts for the fact that the exothermicity of the E-R reaction can lead to breaking of the formed bond.

3.4 Reaction pathway analysis and sensitivity analysis

In order to elucidate the effects of plasma-generated species on the surface chemistry, we carried out a path flux analysis, as presented in the SI (Fig. S6) and the overall picture is summarized in Fig. 8. Indeed, Fig. 8 presents the network of surface reaction pathways for plasma-catalytic CH_4/CO_2 reforming. The thickest arrows represent the contribution of reactions to species formation with time-integrated rates in the order of 10^{-7} mol cm^{-3}, while the thinnest arrows represent the contribution of reactions with time-integrated rates in the order of 10^{-10} mol cm^{-3}. Dashed lines indicate the contribution of reactions with time-integrated rates less than 10^{-10} mol cm^{-3}.
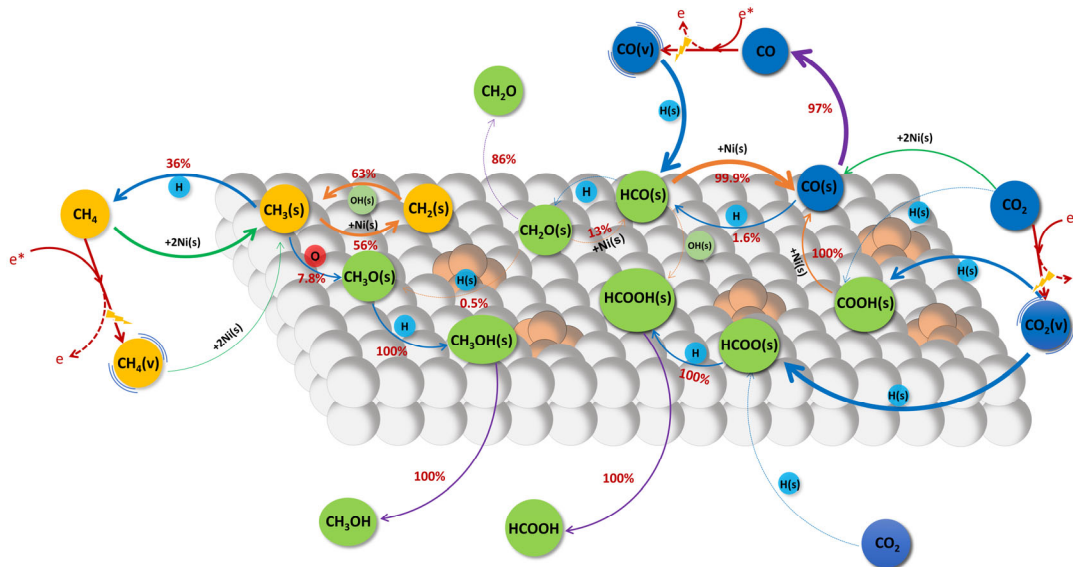
Fig. 8. Network of surface reaction pathways for plasma-catalytic CH_4/CO_2 reforming over Ni-based catalyst (CH_4:CO_2:He = 15:15:70; flow rate: 200 sccm; pressure: 16 kPa; reaction temperature: 473 K; applied voltage: 6000 V; discharge frequency: 20 kHz; pulse duration: 200 ns). (green lines: adsorption or dissociative adsorption reactions; orange lines: L-H reactions; blue lines: E-R reactions; purple lines: desorption reactions)

As shown in Fig. 8, CH_4 is first dissociated on the catalyst surface to produce $CH_3(s)$. The C-H bond rupture on the Ni surface is promoted by exciting the vibrational state of CH_4, which has been verified by state-resolved molecular-beam experiments [64]. In this study, vibrationally excited $CH_4(v)$ contributes for only 1.2% to $CH_3(s)$ formation via the dissociative adsorption reaction: $CH_4(v) + 2Ni(s) \rightarrow CH_3(s) + H(s)$. $CH_3(s)$ is primarily consumed through the E-R reaction: $CH_3(s) + H \rightarrow CH_4 + Ni(s)$, and the surface dehydrogenation (L-H) reaction: $CH_3(s) + Ni(s) \rightarrow CH_2(s) + H(s)$, accounting for 36% and 56% of $CH_3(s)$ consumption, respectively. The remaining $CH_3(s)$ mainly forms $CH_3O(s)$ via the plasma-enhanced E-R reaction: $CH_3(s) + O \rightarrow CH_3O(s)$, which is the predominant formation pathway for $CH_3O(s)$ with a 99.5% contribution. $CH_3O(s)$ further converts to $CH_3OH(s)$ via the hydrogenation reaction $CH_3O(s) + H \rightarrow CH_3OH(s)$. Finally, $CH_3OH(s)$ desorbs from the surface to produce methanol (one of the major oxygenates measured in the experiments; see section 3.1 above), which is the prevalent pathway for CH_3OH formation, as shown in Fig. S6 in the SI.

There are two types of catalytic reactions involving CO_2: the dissociative adsorption of CO_2 on the catalyst surface, as well as the E-R reactions: $CO_2 + H(s) \rightarrow COOH(s)$ and $CO_2 + H(s) \rightarrow HCOO(s)$. The results show that vibrationally excited $CO_2(v)$ significantly accelerates the above E-R reactions, effectively stimulating the formation of $COOH(s)$ and $HCOO(s)$. Almost all of $COOH(s)$ undergoes bond-breaking: $COOH(s) + Ni(s) \rightarrow CO(s) + OH(s)$, to promote the formation of $CO(s)$. As seen in Fig. 8, the desorption reaction: $CO(s) \rightarrow CO + Ni(s)$, is the dominant pathway for $CO(s)$ consumption, accounting for 97% of the total $CO(s)$ consumption, and thus for CO production, which is one of the major products formed (see Fig. 3 above). A small proportion of $CO(s)$ participates in the E-R reaction, $CO(s) + H \rightarrow HCO(s)$, providing only 1.5% of the total $HCO(s)$ formation. Fig. 8 shows that 99% of $HCO(s)$ is formed through the E-R interaction: $CO_2(v) + H(s) \rightarrow HCO(s)$ stimulated by vibrationally excited $CO_2(v)$, highlighting the strong enhancement of vibrationally excited molecules in the surface chemistry. Again, this conclusion is based on certain assumptions in the model, i.e., the so-called α-approximation, namely that the activation barrier is reduced by the value of vibrational energy taken with efficiency α. However, this approximation is subject to uncertainties. Therefore, our conclusion should be considered with caution, and keeping in mind the above model assumptions.

The results show that 99.9% of $HCO(s)$ are dehydrogenated on the catalyst surface, facilitating the formation of $CO(s)$. However, there is an alternative route to consume the remaining $HCO(s)$ with $OH(s)$, via $HCO(s) + OH(s) \rightarrow HCOOH(s) + Ni(s)$, to generate $HCOOH(s)$. Our model predicts that the E-R hydrogenation reaction $HCOO(s) + H \rightarrow HCOOH(s)$ is by far the dominant formation pathway of $HCOOH(s)$. The desorption of $HCOOH(s)$ from the catalyst surface leads to the formation of HCOOH, which is indeed expected to be one of the major oxygenates formed. Note that we could not measure it in this work, due to limitations of the DB-WAX GC column, as mentioned above; but it was one of the major oxygenates detected in our previous study, where we reached good agreement for the HCOOH selectivity between our model and experiments [35]. Furthermore, a very small amount of $HCO(s)$ reacts with H atoms through the E-R reaction, $HCO(s) + H \rightarrow CH_2O(s)$, to generate $CH_2O(s)$, which is an important formation pathway (38%) for $CH_2O(s)$. The majority of $CH_2O(s)$ desorbs from the catalyst surface leading to CH_2O formation, which is one of the major oxygenates detected in our experiments (see section 3.1 above). As we also focus on coking kinetics in this study, the reaction pathways for carbon deposition $C(s)$ on the catalyst surface are depicted in Fig. 10, as well as the catalytic H_2 formation pathways.

To summarize, the path flux analysis shows that E-R reactions dominate the surface reaction pathways in plasma-catalytic DRM, at least based on the assumptions made in the model, which is very different from thermal catalysis, where L-H reactions dominate. In other words, our model indicates that the coupling of catalyst with non-equilibrium plasma can effectively shift the formation and consumption pathways of important adsorbates, highlighting the important role of plasma-generated radicals and vibrationally excited molecules in the surface chemistry, if the assumptions made are indeed valid.

To account for the effect of these assumptions, and to study the kinetic limitations of E-R reactions on the product formation in plasma-catalytic DRM, we also performed a sensitivity analysis, as presented in the SI, section S.6. Fig. S7 demonstrates that the sensitivity coefficients for H_2, C_2H_6, C_2H_4 formation are noticeably smaller compared to those of CO, CH_3OH, and HCOOH. This deviation in the sensitivity coefficients suggests that the influence of E-R reactions on the generation of CO, CH_3OH, and HCOOH is greater than their promotive effects on the production of H_2, C_2H_6, and C_2H_4, which is verified by the reaction path flux analysis for the aforementioned products in Fig. S6 in the SI.

3.5 Coking kinetics analysis

Experimentally, a considerable amount of carbon was deposited on the reactor tube wall and catalyst surface, which might result in unstable plasma discharge and catalyst deactivation. Therefore, we also used our model to

perform a kinetic analysis for carbon deposition in plasma-catalytic DRM.
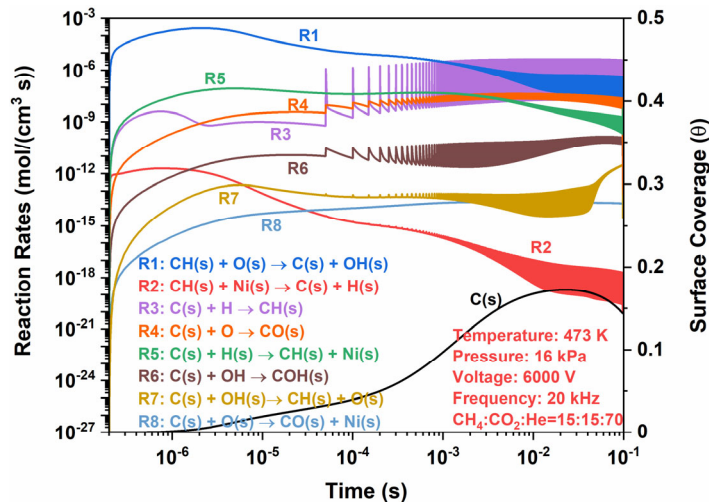
Fig. 9. Time evolution of reaction rates of carbon formation (R1, R2) and elimination (R3-R8) reactions, as well as carbon coverage (C(s)) (CH4:CO2:He = 15:15:70; flow rate: 200 sccm; pressure: 16 kPa; reaction temperature: 473 K; applied voltage: 6000 V; discharge frequency: 20 kHz; pulse duration: 200 ns).

Fig. 9 illustrates the time evolution of the key carbon formation and elimination reaction rates in plasma-catalytic DRM. After the first pulse of the nanosecond-pulsed discharge, the rate of the oxidative dehydrogenation reaction (R1) CH(s) + O(s) → C(s) + OH(s), is approximately 3-4 orders of magnitude higher than that of the carbon elimination reaction (R5) C(s) + H(s) → CH(s) + Ni(s). As the reaction proceeds, plasma-enhanced E-R reactions (R3) C(s) + H → CH(s) and (R4) C(s) + O → CO(s) become the primary carbon elimination reactions. However, the rates of these two reactions are still lower than the rate of the carbon deposition reaction (R1) CH(s) + O(s) → C(s) + OH(s), resulting in a rapid increase in carbon deposition coverage, as indicated by the black curve in Fig. 9. As the coverage of CH(s) decreases, its oxidative dehydrogenation rate decreases as well. Fig. 9 clearly shows that the reaction rate of C(s) + H → CH(s) (R3) becomes higher than that of CH(s) + O(s) → C(s) + OH(s) (R1) after 0.02 s, after which the coverage of carbon gradually decreases again. Thermogravimetric analysis (TGA) was used to determine deposited carbon during plasma-catalytic DRM (cf. SI, Fig. S8). As shown in Fig. S9 in the SI, our kinetic model predicts the trend of selectivity toward carbon deposition as a function of applied voltage and reaction temperature. However, some discrepancies exist between our simulation and experimental results. Given the multiphase nature of the products, accurate quantification of carbon deposition indeed presents significant challenges. While differences in calculated and measured carbon deposition selectivity are not unexpected due to the large number of chemical reactions and uncertainties in rate coefficients, we prefer not to "tune" our model without a real scientific basis. Indeed, all assumptions made in our model are based on logical and plausible physics. Overall, we believe that our model is sufficiently realistic to capture the underlying mechanism of carbon deposition in plasma-catalytic DRM reaction.

Comparing the rates of the main carbon elimination reactions, we can see that the rates of the plasma-enhanced E-R reactions, C(s) + H → CH(s) (R3) and C(s) + O → CO(s) (R4), are several orders of magnitude higher than those of the corresponding L-H reactions, C(s) + H(s) → CH(s) + Ni(s) (R5) and C(s) + O(s) → CO(s) + Ni(s) (R8) after 10^{-3} s. This indicates that the plasma-generated H and O atoms are indeed able to eliminate carbon deposition in plasma catalysis, as predicted by our model, again under the condition that the assumptions made in the model about the role of E-R reactions hold true (see discussion in section 2.2.2 above). Note that we measured no conversion for the thermal catalytic CH4/CO2 reforming due to the low temperature (see section 3.1). While this limits the validation

by experimental data in this study, it aligns with findings reported in the literature by Vakili *et al.* [65] and Shi *et al.* [66].

We also analyzed the carbon formation and consumption in the gas phase, as shown in Fig. S10 and Fig. S11 in the SI. Our model shows that the electron impact dissociation reactions, $e + CH_4 \rightarrow e + C + 2H_2$ and $e + CO \rightarrow e + C + O$, dominate the carbon formation, which is then deposited, $C \rightarrow C_{soot}$, and this process contributes for about 18% to the C(s) formation.
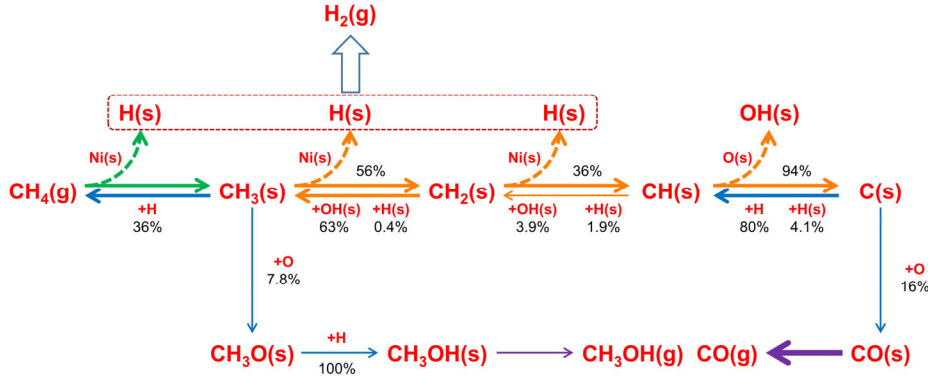
Fig. 10. Network of surface reaction pathways for carbon deposition C(s), and elimination, for plasma-catalytic CH_4/CO_2 reforming over Ni-based catalyst ($CH_4:CO_2:He = 15:15:70$; flow rate: 200 sccm; pressure: 16 kPa; reaction temperature: 473 K; applied voltage: 6000 V; discharge frequency: 20 kHz; pulse duration: 200 ns).

Fig. 10 depicts the predicted surface reaction pathways for carbon deposition and elimination based on our simulation results. The first point to stress is that the E-R reactions, $CH_3(s) + H \rightarrow CH_4 + Ni(s)$ and $CH_3(s) + O \rightarrow CH_3O(s)$, provide additional routes for $CH_3(s)$ consumption to inhibit its complete dehydrogenation to carbon. Continuing from Fig. 8, 63% of $CH_2(s)$ is consumed via the L-H reaction, $CH_2(s) + OH(s) \rightarrow CH_3(s) + O(s)$, while 36% of $CH_2(s)$ undergoes dehydrogenation, $CH_2(s) + Ni(s) \rightarrow CH(s) + H(s)$, yielding CH(s) on the catalyst surface. A significant amount of CH(s) is dehydrogenated via $CH(s) + O(s) \rightarrow C(s) + OH(s)$, resulting in the deposition of carbon C(s), which accounts for 94% of its overall consumption. In summary, the carbon deposition on the catalyst surface is primarily formed through the successive dehydrogenation of CH_4. Note that the nature of the active sites, metal-support interactions, and catalyst morphology all play significant roles in determining the rates and types of carbon deposition. The rational design and screening of catalysts are helpful for controlling carbon deposition during the plasma-catalytic DRM process. Meanwhile, H(s) generated during dehydrogenation further interact with each other through the L-H reaction $H(s) + H(s) \rightarrow H_2 + 2Ni(s)$, resulting in the formation of H_2, a major product, as shown in Fig. 3. In traditional thermal catalytic DRM, the main consumption pathways of carbon deposition C(s) involve oxidative processes: $C(s) + O(s) \rightarrow CO(s) + Ni(s)$, $C(s) + OH(s) \rightarrow CO(s) + H(s)$, and $C(s) + OH(s) \rightarrow COH(s) + Ni(s)$ [67]. However, the consumption pathways are shifted in plasma-catalytic DRM. Plasma-enhanced E-R reactions $C(s) + H \rightarrow CH(s)$ and $C(s) + O \rightarrow CO(s)$ dominate the consumption of carbon deposition C(s), accounting for 80% and 16% of the overall consumption of C(s), respectively.

4. Conclusions and outlook for future work

We studied the plasma-catalytic reforming of CH_4 and CO_2 over a SiO_2-supported Ni catalyst at reduced pressure (8-40 kPa), both experimentally and by chemical kinetics simulations to elucidate the underlying mechanisms, with a particular emphasis on the effects of reactive species on the surface chemistry and coking kinetics. Compared to the plasma reforming without catalyst, plasma catalysis significantly enhances the reactants conversion and products selectivity, demonstrating that the combination of plasma and catalyst enhances the DRM performance. The

experimental measurements show a peak CH_4 and CO_2 conversion of 20% and 11%, respectively. Additionally, we achieved a maximum selectivity of 78% for CO and 75% for H_2, in plasma-catalytic DRM.

Furthermore, our chemical kinetic calculation suggests that vibrationally excited molecules as well as radicals produced in the plasma can accelerate the dissociative adsorption and E-R interactions, promoting the generation of adsorbed species. A path flux analysis shows that E-R reactions dominate the surface reaction pathways in plasma-catalytic DRM, indicating that the coupling of non-equilibrium plasma and catalyst can effectively shift the formation and consumption pathways of important adsorbates. For example, $CH_3O(s)$ and $HCOO(s)$ are mainly generated through the E-R reactions, $CH_3(s) + O \rightarrow CH_3O(s)$ and $CO_2(v) + H(s) \rightarrow HCOO(s)$. Additionally, the hydrogenation reactions $CH_3O(s) + H \rightarrow CH_3OH(s)$ and $HCOO(s) + H \rightarrow HCOOH(s)$ are the main sources of $CH_3OH(s)$ and $HCOOH(s)$, respectively. As the assumptions made in our model on E-R reactions are subject to uncertainties, we also performed a sensitivity analysis, which demonstrates that uncertainties in the rate coefficients of E-R reactions have a more significant influence on the generation of CO, CH_3OH, and HCOOH compared to the formation of H_2, C_2H_6, and C_2H_4.

Further, our model reveals that carbon deposition on the catalyst surface is primarily formed via the oxidative reaction $CH(s) + O(s) \rightarrow C(s) + OH(s)$, while $CH(s)$ is mainly formed through the stepwise dehydrogenation of CH_4. The consumption pathways seem to be the E-R reactions, $C(s) + H \rightarrow CH(s)$ and $C(s) + O \rightarrow CO(s)$, enhanced by plasma-generated H and O atoms, which play a dominant role (ca. 80 and 16%, respectively) in the consumption of carbon deposition $C(s)$, respectively. It is worth noting that compared to thermal catalysis, the E-R reactions, $CH_3(s) + H \rightarrow CH_4 + Ni(s)$ and $CH_3(s) + O \rightarrow CH_3O(s)$, provide additional routes for $CH_3(s)$ consumption to inhibit its complete dehydrogenation to carbon.

To summarize, E-R reactions seem to dominate the surface reaction pathways in plasma-catalytic DRM, if the E-R reactions are indeed correctly described in our model, which is in stark contrast to thermal catalysis, where L-H reactions typically prevail. This finding indicates that the coupling of catalyst with non-equilibrium plasma can effectively shift the formation and consumption pathways of important surface adsorbates, highlighting the effect of plasma-generated radicals and vibrationally excited molecules in the catalytic surface chemistry.

However, there is still room for improvement in this study. We summarize the shortcomings and outline future directions below.

Firstly, while this study focused on the effects of plasma-generated reactive species on the surface chemistry, catalyst design and screening were not emphasized. Future work will delve into catalyst development and operating parameters optimization, particularly at atmospheric pressure, to improve reaction performance in terms of reactant conversion, high-value products selectivity, and energy efficiency.

Secondly, the absence of online or *in situ* measurements hindered the model validation for intermediates and surface species. We will incorporate *in situ* characterization like Fourier transform infrared spectroscopy (FTIR), Laser induced fluorescence (LIF), and online gas chromatography-mass spectrometry (GC-MS), to gain a deeper understanding of the underlying promotive mechanism for plasma-catalyst interactions. Additionally, Transmission electron microscopy (TEM) and other techniques will be combined to characterize the surface alteration of the catalyst during the reaction. Furthermore, TEM and Raman spectroscopy will be employed to characterize the carbon deposition to enhance our understanding of coke formation.

Finally, the developed plasma-enhanced surface mechanism relied on some assumptions, including the α model for plasma-enhanced dissociative adsorption and a zero eV enthalpy barrier for E-R reactions involving radicals/atoms. Although widely accepted, these assumptions may introduce uncertainties in our results. In future work, we will combine DFT or AIMD calculations to provide values for key reaction steps to improve the accuracy of the kinetic model.

Declaration of Competing Interest

The authors declare that they have no known competing financial interests or personal relationships that could have appeared to influence the work reported in this paper.

Acknowledgements

Appendix A. Supporting Information

Supplementary data and mechanism files that support the findings of this study can be found online at https://xxx

ORCID iDs

Jintao Sun https://orcid.org/0000-0003-2053-1506

Qi Chen https://orcid.org/0000-0002-1783-5931

Shangkun Li https://orcid.org/0000-0002-9297-1669

Annemie Bogaerts https://orcid.org/0000-0001-9875-6460

Reference

[1] L. Wang, Y. Yi, C. Wu, H. Guo, X. Tu, One-step reforming of CO_2 and CH_4 into high-value liquid chemicals and fuels at room temperature by plasma-driven catalysis, Angew. Chem. 129 (2017) 13867-13871.

https://doi.org/10.1002/ange.201707131

[2] X. Tu, J. C. Whitehead, Plasma-catalytic dry reforming of methane in an atmospheric dielectric barrier discharge: understanding the synergistic effect at low temperature, Appl. Catal. B Environ. 125 (2012) 439-448.

https://doi.org/10.1016/j.apcatb.2012.06.006

[3] Y. Wang, Y. Chen, J. Harding, H. He, A. Bogaerts, X. Tu, Catalyst-free single-step plasma reforming of CH_4 and CO_2 to higher value oxygenates under ambient conditions, Chem. Eng. J. 450 (2022) 137860.

https://doi.org/10.1016/j.cej.2022.137860

[4] S. Liu, L.R. Winter, J.G. Chen, Review of plasma-assisted catalysis for selective generation of oxygenates from CO_2 and CH_4, ACS Catal. 10 (2020) 2855-2871.

https://dx.doi.org/10.1021/acscatal.9b04811

[5] A. Bogaerts, X. Tu, J.C. Whitehead, G. Centi, L. Lefferts, et al, The 2020 plasma catalysis roadmap, J. Phys. D: Appl. Phys. 53 (2020) 443001.

https://doi.org/10.1088/1361-6463/ab9048

[6] Y. Wang, M. Craven, X. Yu, J. Ding, P. Bryant, J. Huang, X. Tu, Plasma-enhanced catalytic synthesis of ammonia over a Ni/Al_2O_3 catalyst at near-room temperature: insights into the importance of the catalyst surface on the surface mechanism, ACS Catal. 9 (2019) 10780-10793.

https://doi.org/10.1021/acscatal.9b02538

[7] J. Sun, Q. Chen, X. Zhao, H. Lin, W. Qin, Kinetic investigation of plasma catalytic synthesis of ammonia: insights into the role of excited states and plasma-enhanced surface chemistry, Plasma Sources Sci. Technol. 31 (2022) 094009.

https://doi.org/10.1088/1361-6595/ac8e2c

[8] E. Meloni, L. Cafiero, M. Martino, V. Palma, Structured catalysts for non-thermal plasma-assisted ammonia synthesis, Energies, 16(7) (2023) 3218.

https://doi.org/10.3390/en16073218

[9] R. De Meyer, Y. Gorbanev, R. Ciocarlan, P. Cool, S. Bals, A. Bogaerts, Importance of plasma discharge characteristics in plasma

catalysis: dry reforming of methane vs. ammonia synthesis, Chem. Eng. J. 488 (2024) 150838.

https://doi.org/10.1016/j.cej.2024.150838

[10] J.A. Andersen, M.C. Holm, K. van't Veer, J.M. Christensen, M. Østberg, A. Bogaerts, A.D. Jensen, Plasma-catalytic ammonia synthesis in a dielectric barrier discharge reactor: A combined experimental study and kinetic modelling, Chem. Eng. J. 457 (2023) 141294.

https://doi.org/10.1016/j.cej.2023.14294

[11] M. Ronda-Lloret, Y. Wang, P. Oulego, G. Rothenberg, X. Tu, N.R. Shiju, CO_2 hydrogenation at atmospheric pressure and low temperature using plasma-enabled catalysis over supported cobalt oxide catalysts, ACS Sustainable Chem. Eng. 8 (2020) 17397-17407.

https://doi.org/10.1021/acssuschemeng.0c05565

[12] Z. Cui, S. Meng, Y. Yi, A. Jafarzadeh, S. Li, E.C. Neyts, Y. Hao, et al, Plasma-catalytic methanol synthesis from CO_2 hydrogenation over a supported Cu cluster catalyst: insights into the reaction mechanism, ACS Catal. 12 (2022) 1326-1337.

https://doi.org/10.1021/acscatal.1c04678

[13] E. Meloni, L. Cafiero, S. Renda, M. Martino, M. Pierro, V. Palma, Ru- and Rh- based catalysts for CO_2 methanation assisted by non-thermal plasma, Catalysts, 13(3) (2023) 488.

https://doi.org/10.3390/catal13030488

[14] R. Gholami, C.E. Stere, A. Goguet, C. Hardacre, Non-thermal-plasma-activated de-NO_x catalysis, Philos, T. R. Soc. A 376 (2018) 20170054.

https://doi.org/10.1098/rsta.2017.0054

[15] Y. Yi, S. Li, Z. Cui, Y. Hao, Y. Zhang, L. Wang, P. Liu, X. Tu, X. Xu, H. Guo, A. Bogaerts, Selective oxidation of CH_4 to CH_3OH through plasma catalysis: insights from catalyst characterization and chemical kinetics modelling, Appl. Catal. B Environ. 296 (2021) 120384.

https://doi.org/j.apcatb.2021.120384

[16] H. Lv, S. Meng, Z. Cui, S. Li, D. Li, X. Gao, H. Guo, A. Bogaerts, Y. Yi, Plasma-catalytic direct oxidation of methane to methanol over Cu-MOR: revealing the zeolite-confined Cu^{2+} active sites, Chem. Eng. J. 496 (2024) 154337.

https://doi.org/10.1016/j.cej.2024.154337

[17] D. Mei, M. Sun, S. Liu, P. Zhang, Z. Fang, X. Tu, Plasma-enabled catalytic dry reforming of CH_4 into syngas, hydrocarbons and oxygenates: insights into the active metals of γ-Al_2O_3 supported catalysts, J. CO_2 Util. 67 (2023) 102307.

https://doi.org/10.1016/j.jcou.2022.102307

[18] L. Dou, Y. Liu, Y. Gao, J. Li, X. Hu, S. Zhang, K. Ostrikov, T. Shao, Disentangling metallic cobalt sites and oxygen vacancy effects in synergistic plasma-catalytic CO_2/CH_4 conversion into oxygenates, Appl. Catal. B Environ. 318 (2022) 121830.

https://doi.org/10.1016/j.apcatb.2022.121830

[19] L. Wang, Y. Wang, L. Fan, H. Xu, B. Liu, J. Zhang, Y. Zhu, X. Tu, Direct conversion of CH_4 and CO_2 to alcohols using plasma catalysis over Cu/Al(OH)$_3$ catalysts, Chem. Eng. J. 466 (2023) 143347.

https://doi.org/10.1016/j.cej.2023.143347

[20] B. Loenders, R. Michiels, A. Bogaerts, Is a catalyst always beneficial in plasma catalysis? Insights from the many physical and chemical interactions, J. Energy Chem. 85 (2023) 501-533.

https://doi.org/10.1016/j.jechem.2023.06.016

[21] E.C. Neyts, A. Bogaerts, Understanding plasma catalysis through modelling and simulation-a review, J. Phys. D: Appl. Phys. 47 (2014) 224010.

https://doi.org/10.1088/0022-3727/47/22/224010

[22] J. Hong, S. Pancheshnyi, E. Tam, J.J. Lowke, S. Prawer, A.B. Murphy, Kinetic modelling of NH_3 production in N_2-H_2 non-equilibrium atmospheric-pressure plasma catalysis, J. Phys. D: Appl. Phys. 50 (2017) 154005.

https://doi.org/10.1088/1361-6463/aa6229

[23] S. Pancheshnyi, B. Esimann, G. J. M. Hagelaar, L. C. Pitchford, *Computer Code ZDPlasKin*, www.zdplaskin.laplace.univ-tlse.fr,

University of Toulouse, LAPLACE, CNRS-UPS-INP, Toulouse, France, 2008

[24] K. van't Veer, Y. Engelmann, F. Reniers, A. Bogaerts, Plasma-catalytic ammonia synthesis in a DBD plasma: role of microdischarges and their afterglows, J. Phys. Chem. C 124 (2020) 22871-22883.

https://doi.org/10.1021/acs.jpcc.0c05110

[25] Y. Engelmann, K. van't Veer, Y. Gorbanev, E.C. Neyts, W.F. Schneider, A. Bogaerts, Plasma catalysis for ammonia synthesis: a microkinetic modeling study on the contributions of Eley-Ridel reactions, ACS Sustainable Chem. Eng. 9 (2021) 13151-13163.

https://doi.org/10.1021/acssuschemeng.1c02713

[26] Y. Engelmann, P. Mehta, E.C. Neyts, W.F. Schneider, A. Bogaerts, Predicted influence of plasma activation on nonoxidative coupling of methane on transition metal catalysts, ACS Sustainable Chem. Eng. 8 (2020) 6043-6054.

https://dx.doi.org/10.1021/acssuschemeng.0c00906

[27] R. Michiels, Y. Engelmann, A. Bogaerts, Plasma catalysis for CO_2 hydrogenation: unlocking new pathways towards CH_3OH, J. Phys. Chem. C 124 (2020) 25859-25872.

https://dx.doi.org/10.1021/acs.jpcc.0c07632

[28] T.W. Liu, F. Gorky, M.L. Carreon, D.A. Gomez-Gualdron, Plasma radicals as kinetics-controlling species during plasma-assisted catalytic NH_3 formation: support from microkinetic modeling, ACS Sustainable Chem. Eng. 11 (2023) 16749-16763.

https://doi.org/10.1021/acssuschemeng.3c03813

[29] B. Loenders, Y. Engelmann, A. Bogaerts, Plasma-catalytic partial oxidation of methane on Pt(111): a microkinetic study on the role of different plasma species, J. Phys. Chem. C 125 (2021) 2966-2983.

https://dx.doi.org/10.1021/acs.jpcc.0c09849

[30] P. Mehta, P. Barboun, F.A. Herrera, J. Kim, P. Rumbach, D.B. Go, J.C. Hicks, W.F. Schneider, Overcoming ammonia synthesis scaling relations with plasma-enabled catalysis, Nat. Catal. 1 (2018) 269-275.

https://doi.org/10.1038/s41929-018-0045-1

[31] M. Shirazi, E.C. Neyts, A. Bogaerts, DFT study of Ni-catalyzed plasma dry reforming of methane, Appl. Catal. B Environ. 25 (2017) 605-614.

https://doi.org/10.1016 /j.apcatb.2017.01.004

[32] F. Che, J.T. Gray, S. Ha, N. Kruse, S.L. Scott, J. McEwen, Elucidating the roles of electric fields in catalysis: a perspective, ACS Catal. 8 (2018) 5153-5174.

https://doi.org/10.1021/acscatal.7b02899

[33] J. Pan, T. Chen, Y. Guo, Y. Liu, S. Zhang, Y. Liu, T. Shao, Numerical modeling and mechanism investigation of nanosecond-pulsed DBD plasma-catalytic CH_4 dry reforming, J. Phys. D: Appl. Phys. 55 (2022) 035202.

https://doi.org/10.1088/1361-6463/ac2ad8

[34] M. Zhu, A. Zhong, D. Dai, Q. Wang, T. Shao, K. Ostrikov, Surface-induced effects in plasma-catalytic dry reforming of methane: numerical investigation by fluid modeling, J. Phys. D: Appl. Phys. 55 (2022) 355201.

https://doi.org/10.1088/1361-6463/ac74f7

[35] S. Li, J. Sun, Y. Gorbanev, K. van't Veer, B. Loenders, Y. Yi, T. Kenis, Q. Chen, A. Bogaerts, Plasma-assisted dry reforming of CH_4: How small amounts of O_2 addition can drastically enhance the oxygenates production-experiments and insights from plasma chemical kinetics modelling, ACS Sustainable Chem. Eng. 11 (2023) 15373-15384.

https://doi.org/10.1021/acssuschemeng.3c04352

[36] K.W. Engeling, J. Kruszelnick, M.J. Kushner, J.E. Foster, Time-resolved evolution of micro-discharges, surface ionization waves and plasma propagation in a two-dimensional packed bed reactor, Plasma Sources Sci. Technol. 27 (2018) 085002.

https://doi.org/10.1088/1361-6595/aad2c5

[37] B. Wanten, R. Vertongen, R. De Meyer, A. Bogaerts, Plasma-based CO_2 conversion: how to correctly analyze the performance? J. Energy Chem. 86 (2023) 180-196.

https://doi.org/10.1016/j.jechem.2023.07.005

[38] X. Mao, Q. Chen, A.C. Rousso, T.Y. Chen, Y. Ju, Effects of controlled non-equilibrium excitation on $H_2/O_2/He$ ignition using a hybrid repetitive nanosecond and DC discharge, Combust. Flame 206 (2019) 522-535.
https://doi.org/10.1016/j.combustflame.2019.05.027

[39] A.E. Lutz, R.J. Kee, J.A. Miller, SENKIN: a FORTRAN program for predicting homogeneous gas phase chemical kinetics with sensitivity analysis, *Report NO SAND-87-8248*, 1988 (Livermore, CA: Sandia National Laboratories)

[40] G.J.M. Hagelaar, L.C. Pitchford, Solving the Boltzmann equation to obtain electron transport coefficients and rate coefficients for fluid models, Plasma Sources Sci. Technol. 14 (2005) 722-33.
https://doi.org/10.1088/0963-0252/14/4/011

[41] K. van't Veer, F. Reniers, A. Bogaerts, Zero-dimensional modeling of unpacked and packed bed dielectric barrier discharges: the role of vibrational kinetics in ammonia synthesis, Plasma Sources Sci. Technol. 29 (2020) 045020.
https://doi.org/10.1088/1361-6595/ab7a8a

[42] E. Morais, A. Bogaerts, Modelling the dynamics of hydrogen synthesis from methane in nanosecond-pulsed plasmas, Plasma Process. Polym. 21 (2024) 2300149.
https://doi.org/10.1002/ppap.202300149

[43] J. Sun, Q. Chen, X. Yang, B.E. Koel, Effects of non-equilibrium excitation on methane oxidation in a low-temperature RF discharge, J. Phys. D: Appl. Phys. 53 (2020) 064001.
https://doi.org/10.1088/1361-6463/ab57dc

[44] J. Sun, Q. Chen, B. Zhao, C. Guo, J. Liu, M. Zhang, D. Li, Temperature-dependent ion chemistry in nanosecond discharge plasma-assisted CH_4 oxidation, J. Phys. D: Appl. Phys. 55 (2022) 135203.
https://doi.org/10.1088/1361-6463/ac45ac

[45] J. Sun, Q. Chen, Y. Guo, Z. Zhou, Y. Song, Quantitative behavior of vibrational excitation in AC plasma assisted dry reforming of methane, J. Energy Chem. 46 (2020) 133-143.
https://doi.org/10.1016/j.jechem.2019.11.002

[46] J.A. Manion, R.E. Huie, R.D. Levin, Jr.D.R. Brugess, V.L. Orkin, NIST Chemical Kinetics Database, NIST Standard Reference Database 17, Version 7.0 (Web Version), Release 1.6.8, Data version 2015.09, National Institute of Standards and Technology, Gaithersburg, Maryland, 20899-8320. https://kinetics.nist.gov/

[47] M. Grofulović, L.L. Alves, V. Guerra, Electron-neutral scattering cross sections for CO_2: a complete and consistent set and an assessment of dissociation, J. Phys. D: Appl. Phys. 49 (2016) 395207.
https://doi.org/10.1088/0022-3727/49/39/395207

[48] Hayashi database, (available at: www.lxcat.net) (retrieved on October 17, 2022)

[49] A. Bogaerts, G. Centi, Plasma technology for CO_2 conversion: a personal perspective on prospects and gaps, Front. Energy Res. 8 (2020) 111.
https://doi.org/10.3389/fenrg.2020.00111

[50] R. Snoeckx, A. Bogaerts, Plasma technology-a novel solution for CO_2 conversion? Chem. Soc. Rev. 46 (2017) 5805-5863.
https://doi.org/10.1039/C6CS00066E

[51] J.F. Noxon, Optical emission from $O(^1D)$ and $O_2(b^1\Sigma_g)$ in ultraviolet photolysis of O_2 and CO_2, J. Chem. Phys. 52 (1970) 1852-1873.
https://doi.org/10.1063/1.1673227

[52] T.G. Slanger, G. Black, $O(^1S)$ interactions-the product channels, J. Chem. Phys. 68 (1978) 989-997.
https://doi.org/10.1063/1.435838

[53] J. Sun, Q. Chen, Kinetic roles of vibrational excitation in RF plasma assisted methane pyrolysis, J. Energy Chem. 39 (2019) 188-197.
https://doi.org/10.1016/j.jechem.2019.01.028

[54] A. Fridman, *Plasma Chemistry*, Cambridge University, Cambridge, 2008.

[55] O. Mohan, S. Shambhawi, R. Xu, A.A. Lapkin, S.H. Mushrif, Investigating CO_2 methanation on Ni and Ru: DFT assisted microkinetic analysis, ChemCatChem, 13 (2021) 2420-2433.

http://doi.org/10.1002/cctc.202100073

[56] Y.A. Zhu, D. Chen, X.G. Zhou, W.K. Yuan, DFT studies of dry reforming of methane on Ni catalyst, Catal. Today 148 (2009) 260-267.

https://doi.org/10.1016/j.cattod.2009.08.022

[57] C. Fan, Y.A. Zhu, M.L. Yang, Z.J. Sui, X.G. Zhou, D. Chen, Density functional theory-assisted microkinetic analysis of methane dry reforming on Ni catalyst, Ind. Eng. Chem. Res. 54 (2015) 5901-5913.

https://doi.org/10.1021/acs.iecr.5b00563

[58] T.W. Liu, F. Corky, M.L. Carreon, D.A. Gómez-Gualdrón, Energetics of reaction pathways enabled by N and H radicals during catalytic, plasma-assisted NH_3 synthesis, ACS Sustainable Chem. Eng. 10 (2022) 2034-2051.

https://doi.org/10.1021/acssuschemeng.1c05660

[59] C.T. Campbell, L.H. Sprowl, L. Árnadóttir, Equilibrium constants and rate constants for adsorbates: two-dimensional (2D) ideal gas, 2D ideal lattice gas, and ideal hindered translator models, J. Phys. Chem. C 120 (2016) 10283-10297.

https://dx.doi.org/10.1021/acs.jpcc.6b00957

[60] C.T. Campbell, J.R.V. Sellers, The entropies of adsorbed molecules, *J. Am. Chem. Soc.* 134 (2012) 18109-18115.

https://dx.doi.org/10.1021/ja30801171

[61] M. Kosari, S. Askari, A.M. Seavad, S. Xi, S. Kawi, A. Borgna, H.C. Zeng, Strong coke-resistivity of spherical hollow Ni/SiO_2 catalysts with shell-confined high-content Ni nanoparticles for methane dry reforming with CO_2, Appl. Catal. B Environ. 310 (2022) 121360.

https://doi.org/10.1016/j.apcatb.2022.121360

[62] Y. Shi, Y. Li, S. Wang, Y. Chu, H. Yu, T. Li, H. Yin, Impact of nickel phosphides over Ni/SiO_2 catalysts in dry methane reforming, Catal. Letters 153 (2023) 2787-2802.

https://doi.org/10.1007/s10562-022-04199-6

[63] R. Michiels, E. Neyts, A. Bogaerts, Plasma catalysis modeling: how ideal is atomic hydrogen for Eley-Rideal? J. Phys. Chem. C 128 (2024) 11196-11209.

https://doi.org/10.1021/acs.jpcc.4c02193

[64] L.B.F. Juurlink, D.R. Killelea, A.L. Utz, State-resolved probes of methane dissociation dynamics, Prog. Surf. Sci. 84 (2009) 69-134.

https://doi.org/10.1016/j.progsurf.2009.10.001

[65] R. Vakili, R. Gholami, C.E. Stere, S. Chansai, H. Chen, S.M. Holmes, Y. Jiao, C. Hardacre, X. Fan, Plasma-assisted catalytic dry reforming of methane (DRM) over metal-organic frameworks (MOFs)-based catalysts, Appl. Catal. B Environ. 260 (2020) 118195.

https://doi.org/10.1016/j.apcatb.2019.118195

[66] C. Shi, S. Wang, X. Ge, S. Deng, B. Chen, J. Shen, A review of different catalytic systems for dry reforming of methane: conventional catalysis-alone and plasma-catalytic system, J. CO_2 Util. 46 (2021) 101462.

https://doi.org/10.1016/j.jcou.2021.101462

[67] Z. Wang, X.M. Cao, J. Zhu, P. Hu, Activity and coke formation of nickel and nickel carbide in dry reforming: a deactivation scheme from density functional theory, J. Catal. 311 (2014) 469-480.

https://doi.org/10.1016/j.jcat.2013.12.015

Supporting Information:

Plasma-catalytic dry reforming of CH₄: Effects of plasma-generated species on the surface chemistry

Jintao Sun[1], Qi Chen[1]*, Wanyue Qin[1], Hanyu Wu[2], Bowen Liu[2], Shangkun Li[3], Annemie Bogaerts[3]

1. School of Mechanical, Electronic and Control Engineering, Beijing Jiaotong University, Beijing 100044, China

2. College of Chemical Engineering and Environment, China University of Petroleum-Beijing, Beijing 102249, China

3. Research Group PLASMANT, Department of Chemistry, University of Antwerp, Wilrijk 2610, Belgium

*Corresponding author

E-mail address: qchen@bjtu.edu.cn

Section S.1. Preparation and characterization of the catalyst

Silicon dioxide (Aladdin, analytical grade, 20 nm) and $Ni(NO_3)_2 \cdot 6H_2O$ (Aladdin, analytical grade) are used as the support and metal precursor, respectively, to prepare a 10 wt.% Ni/SiO_2 catalyst using the incipient wetness impregnation method. $Ni(NO_3)_2 \cdot 6H_2O$ and the corresponding quantity of SiO_2 ($m(Ni):m(SiO_2)$ = 1:9) are added to deionized water. To fully dissolve the support and precursor, the solution is continuously stirred at 60 ℃ for 2 h and then stirred at room temperature for 12 h. Afterward, the solution is heated to 85 ℃ to evaporate the water until a slurry is formed. After drying by a baking oven at 110 ℃ for 5 h and calcining in a muffle oven at 500 ℃ for 5 h, the sample is reduced with a 0.95 N_2/0.05 H_2 (100 mL/min) mixture at 550 ℃ for 8 h and then sieved to 40-60 mesh. The catalyst is noted as a 10 wt.% Ni/SiO_2 catalyst. The morphology and surface electronic properties of the catalyst are characterized by H_2 temperature-programmed reduction (H_2-TPR, Micromeritics, AutoChem II 2920), X-ray diffraction (XRD, Rigaku, ULTIMA IV, 3 kW), and X-ray photoelectron spectroscopy (XPS, Thermo Fisher Scientific, K-Alpha⁺, 12 kV).
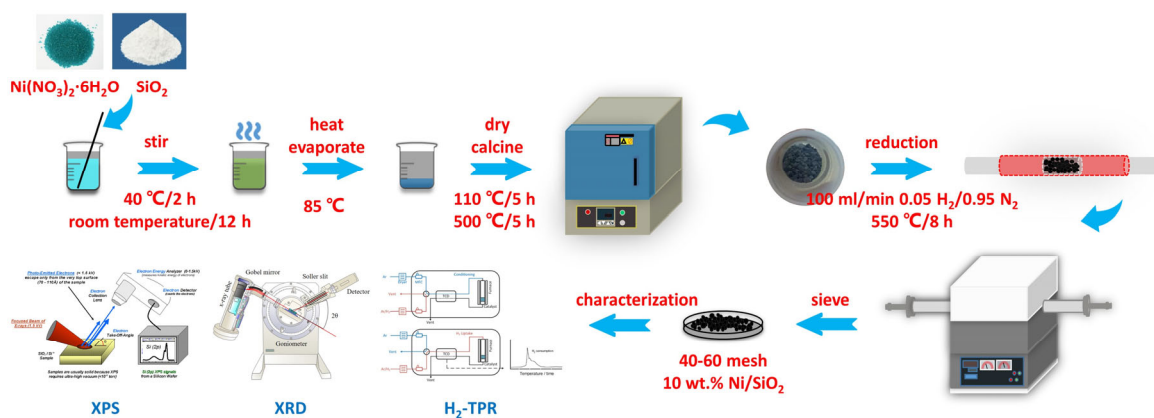
Fig. S1. Schematic diagram of the preparation of Ni/SiO_2 catalyst

To shed light on the distinctive role of the Ni-based catalysts in the plasma-catalytic DRM process, we characterized the Ni/SiO_2 catalyst using XRD, H_2-TPR, and XPS. Fig. S2(a) depicts the XRD spectrum of the Ni/SiO_2 catalyst after H_2 reduction. The diffraction peaks centered at 2θ = 44.43 º, 51.78 º, and 76.26º correspond to the characteristic peaks of metallic Ni, signifying that the loaded metal species predominantly exist on the SiO_2 support surface in the metal state after H_2 reduction. The H_2-TPR profile of the Ni/SiO_2 catalyst prior to thermal

reduction is presented in Fig. S2(b). Two striking reduction peaks within the temperature range of 100-200 °C and 350-500 °C, ascribed to the reduction of bulk NiO (without interaction with SiO_2) and α-phase NiO (weak oxide-support interaction), respectively [1]. The evaluation of H_2-TPR underscores that the Ni/SiO_2 catalyst can be fully reduced under the atmosphere at 550 °C, which aligns with the XRD analysis.

The XPS spectra for Ni 2p of the Ni/SiO_2 catalyst after reduction are shown in Fig. S2(c). Two peaks are detected with binding energy of 852.76 eV and 869.87 eV, attributed to Ni $2p_{3/2}$ and Ni $2p_{1/2}$ of Ni^0 species, respectively, suggesting the presence of metallic Ni species on the surface of the fresh Ni/SiO_2 catalyst. In addition, peaks appearing at 856.14 eV and 873.57 eV are assigned to Ni^{2+} species. The presence of Ni^{2+} species is further confirmed by the appearance of oscillating satellite peaks at 860.76 eV and 878.62 eV. The XPS results indicate that Ni exists on the surface of Ni/SiO_2 in the form of both Ni^0 and Ni^{2+}, and the proportion of Ni^0 is determined to be 49.6%, which is the primarily active species for the activity in DRM.
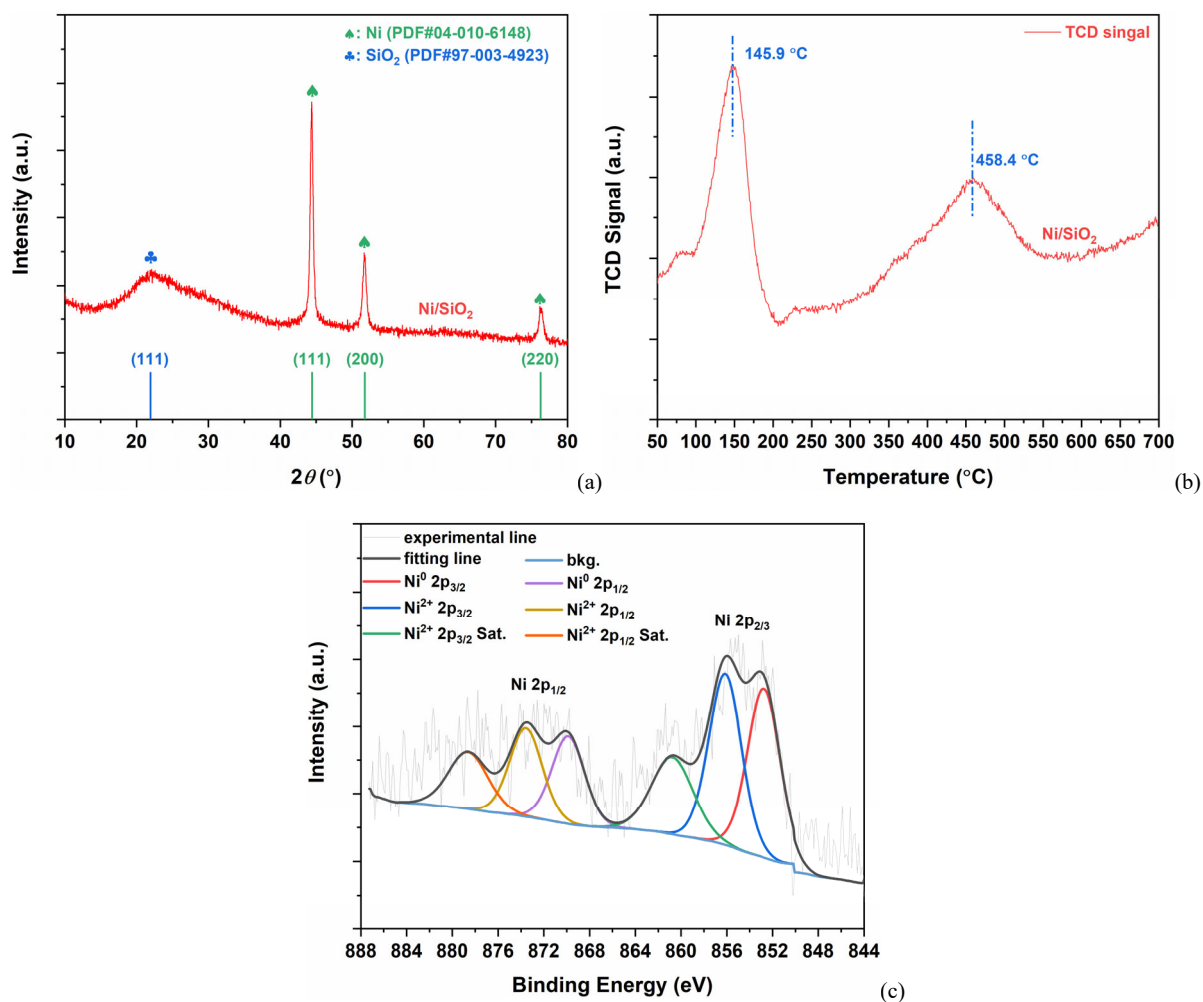
Fig. S2. Characterization of the Ni/SiO_2 catalyst: (a) XRD patterns (after reduction); (b) H_2-TPR profiles (before reduction); (c) Ni 2p XPS spectra (after reduction).

Section S.2. Calculation of reactant conversion and product selectivity

The conversion of CH_4 (X_{CH4}) and CO_2 (X_{CO2}) is defined as [2,3]:

$$X_{CH_4}(\%) = \frac{y_{CH_4}^{in} - \alpha \cdot y_{CH_4}^{out}}{y_{CH_4}^{in}} \times 100\% \tag{S1}$$

$$X_{CO_2}(\%) = \frac{y_{CO_2}^{in} - \alpha \cdot y_{CO_2}^{out}}{y_{CO_2}^{in}} \times 100\% \tag{S2}$$

where y_i^{in} and y_i^{out} ($i = CH_4$, CO_2) are the inlet and outlet reactant mole fractions, respectively. α accounts for the changes in the gas composition and molar flow rate. N_2 is used as an internal standard and added to the gas mixture after the reactor outlet for plasma on and off conditions.

$$\alpha = \frac{y_{plasma}^{off}}{y_{plasma}^{on}} + \beta \left(\frac{y_{plasma}^{off}}{y_{plasma}^{on}} - 1 \right) \tag{S3}$$

Here the factor β is defined as the flow rate of the internal standard with respect to the flow rate at the reactor inlet.

The measured ratio $\dfrac{y_{plasma}^{off}}{y_{plasma}^{on}}$ corresponds to the molar flow changes from chemical reactions while the term

'$\beta \left(\dfrac{y_{plasma}^{off}}{y_{plasma}^{on}} - 1 \right)$' accounts for molar flow changes from the dilution.

The selectivity of gaseous products is calculated as [2,3]:

$$S_{CO}(\%) = \frac{\alpha \cdot y_{CO}^{out}}{\left(y_{CH_4}^{in} - \alpha \cdot y_{CH_4}^{out} \right) + \left(y_{CO_2}^{in} - \alpha \cdot y_{CO_2}^{out} \right)} \times 100\% \tag{S4}$$

$$S_{H_2}(\%) = \frac{2 \cdot \alpha \cdot y_{H_2}^{out}}{4 \cdot \left(y_{CH_4}^{in} - \alpha \cdot y_{CH_4}^{out} \right)} \times 100\% \tag{S5}$$

$$S_{C_xH_y}(\%) = \frac{x \cdot \alpha \cdot y_{C_xH_y}^{out}}{\left(y_{CH_4}^{in} - \alpha \cdot y_{CH_4}^{out} \right) + \left(y_{CO_2}^{in} - \alpha \cdot y_{CO_2}^{out} \right)} \times 100\% \tag{S6}$$

Carbon deposition was determined based on thermogravimetric analysis (TGA), and the selectivity of the oxygenates $C_xH_yO_z$ is calculated as:

$$S_{C_xH_yO_z,total}(\%) = 100\% - S_{CO} - S_{C_xH_y} - S_{C_{carbon}} \tag{S7}$$

$$S_{CH_2O}(\%) = \frac{\alpha \cdot y_{CH_2O}^{out}}{\left(y_{CH_4}^{in} - \alpha \cdot y_{CH_4}^{out} \right) + \left(y_{CO_2}^{in} - \alpha \cdot y_{CO_2}^{out} \right)} \times 100\% \tag{S8}$$

$$S_{CH_3OH}(\%) = \frac{\alpha \cdot y_{CH_3OH}^{out}}{\left(y_{CH_4}^{in} - \alpha \cdot y_{CH_4}^{out} \right) + \left(y_{CO_2}^{in} - \alpha \cdot y_{CO_2}^{out} \right)} \times 100\% \tag{S9}$$

The total conversion is defined as the weighted average of the conversion for each reactant, weighted over their concentration in the inlet gas mixture.

$$\chi^{tot} = c_{CH_4} \cdot \chi_{CH_4} + c_{CO_2} \cdot \chi_{CO_2} \tag{S10}$$

The yields of H₂, CO, hydrocarbons, and oxygenates are defined as:

$$Y_{H_2}(\%) = \frac{\alpha \cdot y_{H_2}^{out}}{2 \cdot y_{CH_4}^{in}} \times 100\% \tag{S11}$$

$$Y_{CO}(\%) = \frac{\alpha \cdot y_{CO}^{out}}{y_{CH_4}^{in} + y_{CO_2}^{in}} \times 100\% \tag{S12}$$

$$Y_{C_xH_y}(\%) = \frac{x \cdot \alpha \cdot y_{C_xH_y}^{out}}{y_{CH_4}^{in} + y_{CO_2}^{in}} \times 100\% \tag{S13}$$

$$Y_{C_xH_yO_z}(\%) = \frac{x \cdot \alpha \cdot y_{C_xH_yO_z}^{out}}{y_{CH_4}^{in} + y_{CO_2}^{in}} \times 100\% \tag{S14}$$

Section S.3. Total conversion and yields
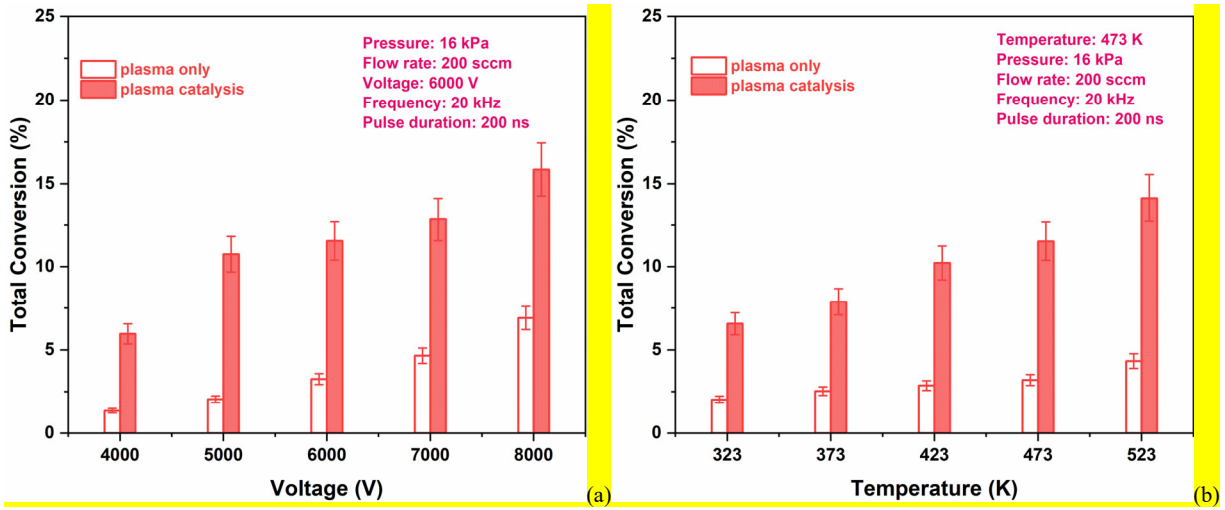
Fig. S3. Experimentally measured total conversion as a function of (a) applied voltage and (b) reaction temperature in plasma-catalytic DRM.
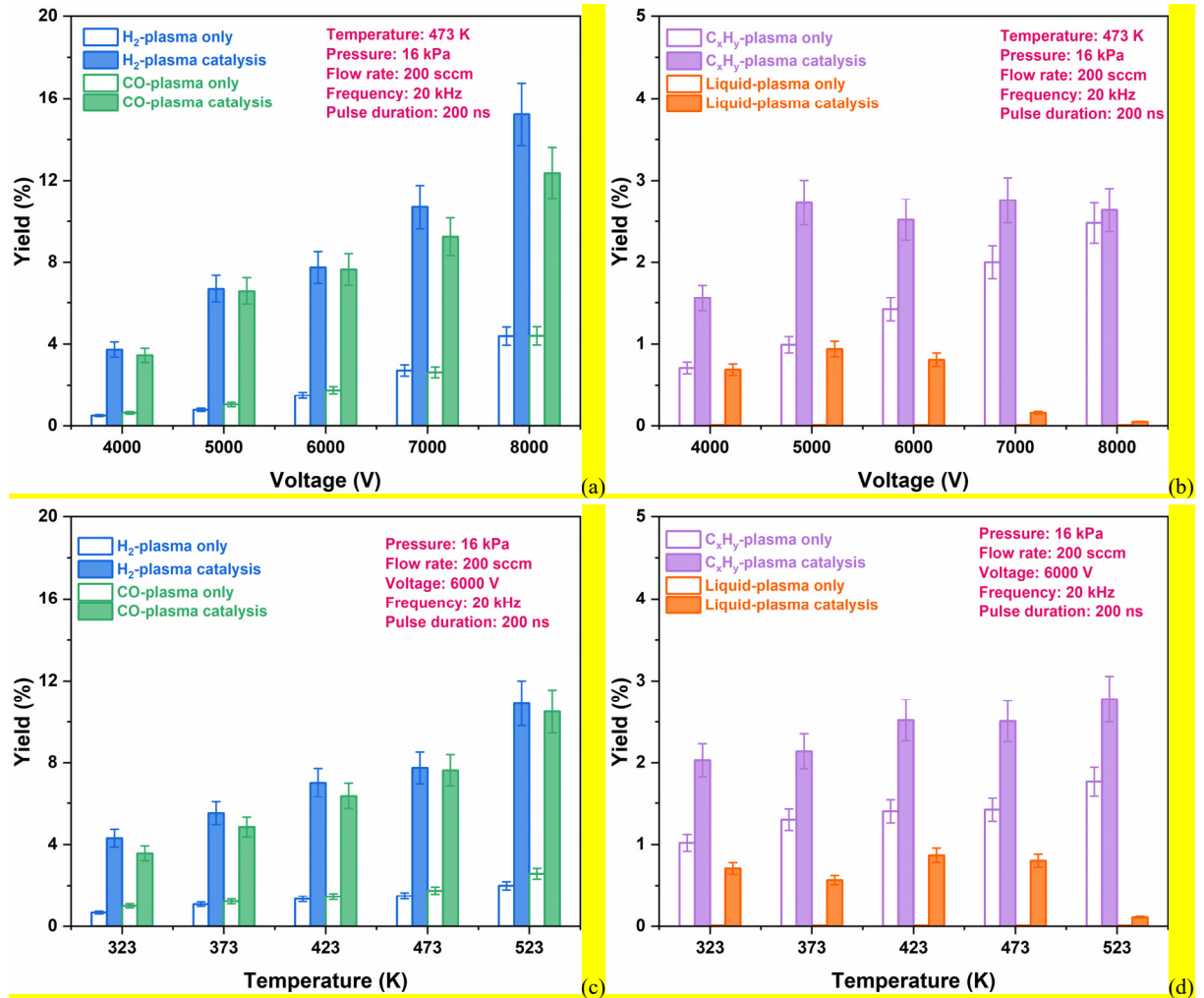
Fig. S4. Effects of applied voltage (a,b) and reaction temperature (c,d) on syngas (a,c) hydrocarbons and oxygenates (b,d) yields.

Section S.4. Optical emission spectra
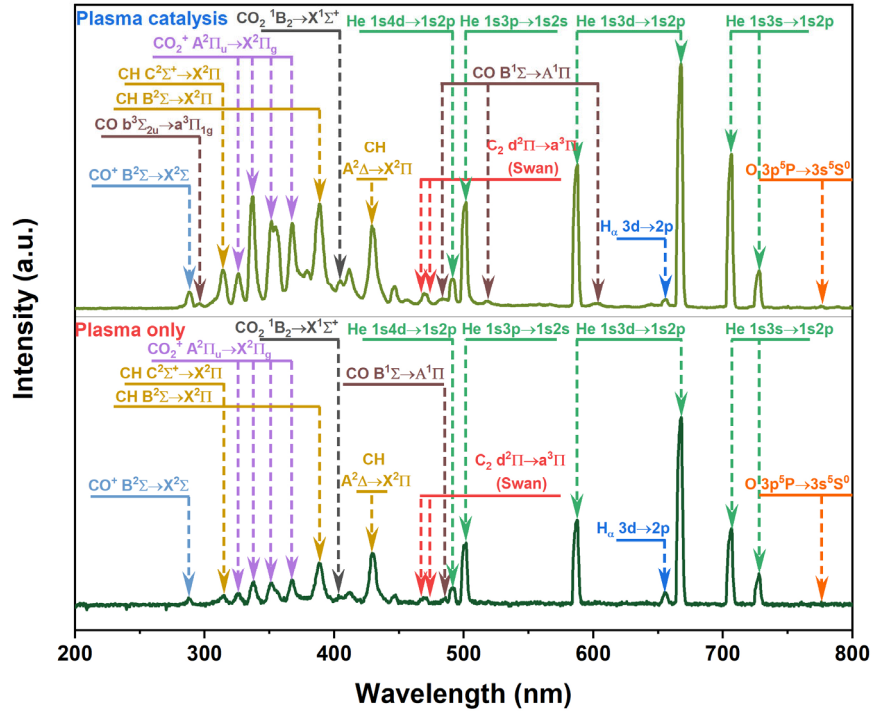
Fig. S5. Optical emission spectra of 0.70 He/0.15 CH$_4$/0.15 CO$_2$ plasma: (a) plasma only and (b) packed with Ni/SiO$_2$ catalyst at applied voltage of 6000 V.

Table S1. Spectroscopic characteristics of the main species detected in the He/CH$_4$/CO$_2$ plasma

Species	Electron transition	Wavelength (nm)	Ref.
He	1s4d→1s2p	492	4
	1s3p→1s2s	502	5
	1s3d→1s2p	588	5
		668	5
	1s3s→1s2p	709	5
		728	5
CO$_2^+$	A$^2\Pi_u$→X$^2\Pi_g$	326	6
		338	6
		351	6
		368	6
CH	C$^2\Sigma^+$→X$^2\Pi$	314	6
	B$^2\Sigma$→X$^2\Pi$	387	6
	A$^2\Delta$→X$^2\Pi$	431	6
CO	b$^3\Sigma_{2u}$→a$^3\Pi_{1g}$	297	6
	B$^1\Sigma$→A$^1\Pi$	483	6
		519	6
		608	6

CO_2	$^1B_2 \rightarrow X^1\Sigma^+$	403	5
CO^+	$B^2\Sigma \rightarrow X^2\Sigma$	289	6
C_2	$d^2\Pi \rightarrow a^3\Pi$ (Swan band)	468-474	6
O	$3p^5P \rightarrow 3s^5S^0$	777	7
H_α	$3d \rightarrow 2p$	656	6

Section S.5. Path flux analysis

As the applied voltage and temperature rise, the reduced electric field (E/N) increases correspondingly, enhancing the electron impact dissociation of CO_2, CH_4, and C_2H_6. This facilitates CO formation while suppressing C_2H_6 formation (see Table S2) and the competitive reaction $CH_4 + CH \rightarrow C_2H_4 + H$ (the dominant C_2H_4 formation pathway, see Fig. S6 and Table S3), leading to reduced hydrocarbons selectivity. On the other hand, the increasing E/N inhibits the main CH_3OH formation pathways, $O(^1D) + CH_4 \rightarrow CH_3OH$, and the formation of $CH_3(s)$ (the precursor of $CH_3OH(s)$, see Fig. 8), due to the competition with electron impact reactions of CH_4 (see Table S3). Additionally, increasing E/N leads to a decrease in the electron energy deposited into the CO_2 vibrational excitation channel, thereby reducing HCOOH formation via the catalytic mechanism: $CO_2(v) \rightarrow HCOO(s) \rightarrow HCOOH(s) \rightarrow$ HCOOH (see Fig. 8). Therefore, increasing the applied voltage and temperature lowers the selectivity for oxygenates.

Table S2. C_2H_6 consumption pathways in plasma-catalytic DRM (6000 V, 473 K)

Reaction	Time-integrated reaction rate (mol/cm³)	Contribution
$e + C_2H_6 \rightarrow e + C_2H_4 + H_2$	2.80×10^{-9}	42.8%
$e + C_2H_6 \rightarrow e + C_2H_5 + H$	9.39×10^{-10}	14.3%
$e + C_2H_6 \rightarrow e + C_2H_2 + H_2 + H_2$	5.65×10^{-10}	8.6%
$e + C_2H_6 \rightarrow e + CH_3 + CH_3$	3.96×10^{-10}	6.1%
$O(^1D) + C_2H_6 \rightarrow C_2H_5OH$	3.86×10^{-10}	5.9%
$e + C_2H_6 \rightarrow e + CH_4 + CH_2$	3.06×10^{-10}	4.7%
$C_2H_6 + OH \rightarrow C_2H_5 + H_2O$	2.97×10^{-10}	4.5%
$O(^1D) + C_2H_6 \rightarrow C_2H_5 + OH$	2.44×10^{-10}	3.7%
$C_2H_6 + CH \rightarrow C_2H_4 + CH_3$	2.41×10^{-10}	3.7%
$e + C_2H_6 \rightarrow e + C_2H_3 + H_2 + H$	9.61×10^{-11}	1.5%
$C_2H_6 + O \rightarrow C_2H_5 + OH$	7.31×10^{-11}	1.1%

Table S3. CH_4 consumption pathways in plasma-catalytic DRM (6000 V, 473 K)

Reaction	Time-integrated reaction rate (mol/cm³)	Contribution
$e + CH_4 \rightarrow e + CH_4(v)$	7.70×10^{-7}	69.1%
$e + CH_4 \rightarrow e + CH_3 + H$	1.20×10^{-7}	10.8%
$e + CH_4 \rightarrow e + CH_2 + H_2$	5.20×10^{-8}	4.7%
$CH_4 + 2Ni(s) \rightarrow CH_3(s) + H(s)$	5.03×10^{-8}	4.5%
$e + CH_4 \rightarrow e + CH + H_2 + H$	2.30×10^{-8}	2.1%
$CH_4 + CH \rightarrow C_2H_4 + H$	1.95×10^{-8}	1.8%
$e + CH_4 \rightarrow e + C + H_2 + H_2$	1.65×10^{-8}	1.5%
$CH_4^+ + CH_4 \rightarrow CH_5^+ + CH_3$	1.50×10^{-8}	1.4%
$O(^1D) + CH_4 \rightarrow CH_3 + OH$	9.98×10^{-9}	0.9%
$e + CH_4 \rightarrow 2e + CH_4^+$	9.45×10^{-9}	0.8%
$CO_2^+ + CH_4 \rightarrow CH_4^+ + CO_2$	5.09×10^{-9}	0.5%
$CH_3^+ + CH_4 \rightarrow C_2H_5^+ + H_2$	4.81×10^{-9}	0.4%
$e + CH_4 \rightarrow 2e + CH_3^+ + H$	3.55×10^{-9}	0.3%
$O(^1D) + CH_4 \rightarrow CH_3OH$	3.43×10^{-9}	0.3%

CH₄ + OH → CH₃ + H₂O	3.26×10⁻⁹	0.3%
O(¹D) + CH₄ → CH₂OH + H	2.35×10⁻⁹	0.2%
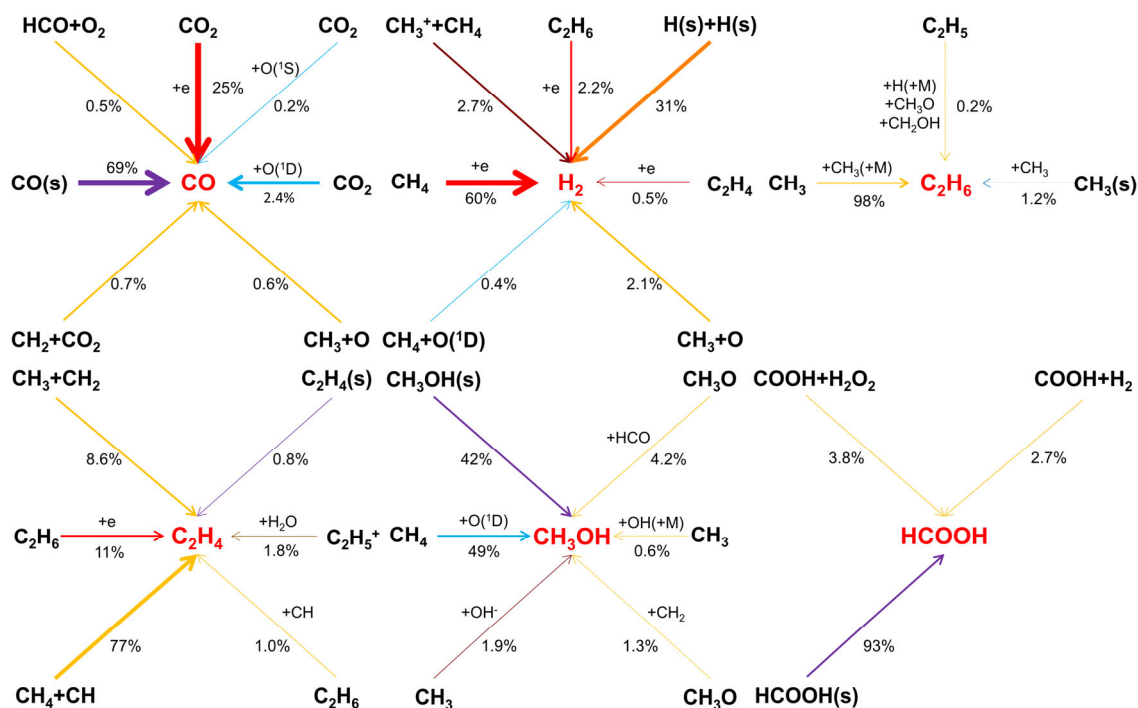
Fig. S6. Reaction path flux analysis for CO, H₂, C₂H₆, C₂H₄, CH₃OH and HCOOH for a 0.15 CH₄/0.15 CO₂/0.70 He mixture at a pressure of 16 kPa, and temperature of 473 K. (red lines: electron impact reactions; yellow lines: chain reactions; light blue lines: chain reactions accelerated by excited species; brown lines: ionic reactions; orange lines: L-H reactions; blue lines: E-R reactions; purple lines: desorption reactions)

Section S.6. Sensitivity analysis

We introduced three additional free energy barriers (0.2 eV, 0.4 eV, 0.6 eV) to the E-R reactions, and the rate constants, $k_{ER,0}$ for E-R reactions with consideration of the enthalpy barrier are calculated with the formula,

$$k_{ER,0} = k_{ER} \exp\left(-E_{ER}/RT\right) \tag{S10}$$

where, k_{ER} is the rate constants for the E-R reactions calculated by eq. (5); and E_{ER} is the assumed additional enthalpy barrier.

To explore the consequences of the assumed E-R rates for these steps on the product concentrations, we calculated the sensitivity coefficient. The definition of logarithmic sensitivity coefficient pS [8] is as follows,

$$pS = \frac{\log\left(Conc'/Conc\right)}{\log\left(k_j'/k_j\right)} \tag{S11}$$

where, k_j' and k_j are the rate coefficients for the jth E-R reaction with and without activation enthalpy considered, respectively. Correspondingly, $Conc'$ and $Conc$ represent the product concentrations with and without consideration of the activation enthalpy for the jth E-R reaction. Positive and negative values of the sensitivity coefficient indicate the promoting and inhibiting effects for the corresponding E-R reaction on the product formation, respectively.
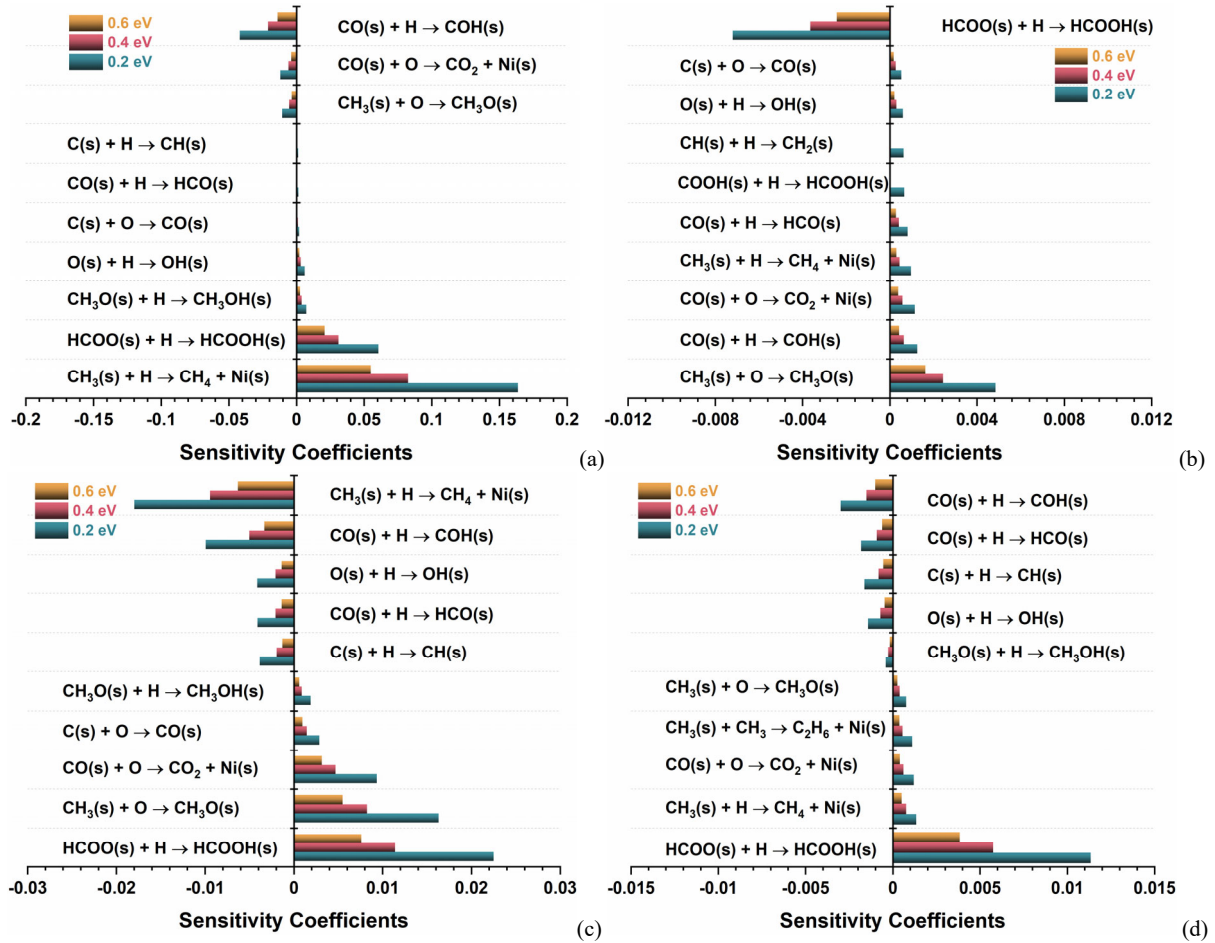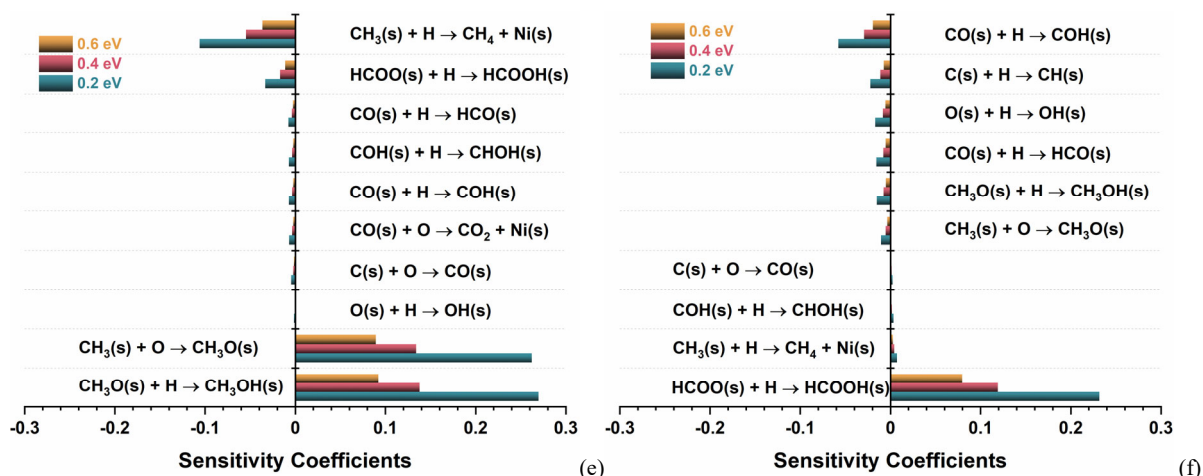
Fig. S7(a) shows that the hydrogenation reaction $CH_3(s) + H \rightarrow CH_4 + Ni(s)$ exhibits the most noticeable promoting effect on CO formation. As revealed in Fig. 8, this process is the important pathway for $CH_3(s)$ consumption, leading to the regeneration of active sites Ni(s). This, in turn, promotes the formation of CO(s) through the dehydrogenation of HCO(s), which eventually leads to the production of CO via the desorption of CO(s). Furthermore, the reactions $HCOO(s) + H \rightarrow HCOOH(s)$ and $CH_3O(s) + H \rightarrow CH_3OH(s)$ also present a strong promoting effect on CO production. These processes are also applicable to the similar promotion mechanism, regenerating active sites to promote the L-H reaction $HCO(s) + Ni(s) \rightarrow CO(s) + H(s)$. In contrast, the E-R reaction $CO(s) + H \rightarrow COH(s)$ exhibits the highest negative sensitivity because it is a minor pathway for CO(s) consumption. Meanwhile, another consumption process for CO(s) through the reaction $CO(s) + O \rightarrow CO_2 + Ni(s)$ shows an inhibitory effect on CO production. The strong negative sensitivity of the reaction $CH_3(s) + O \rightarrow CH_3O(s)$ towards CO generation is due to its competition with the E-R reaction $CH_3(s) + H \rightarrow CH_4 + Ni(s)$ for the consumption of $CH_3(s)$.

As illustrated in Fig. S7(b), the oxidation reaction of $CH_3(s)$ with O, yielding $CH_3O(s)$, exhibits the highest positive sensitivity coefficient for the formation of H₂. The produced $CH_3O(s)$ enhances the formation of $CH_3OH(s)$ through the hydrogenation pathway, facilitating the regeneration of active sites Ni(s) due to the relatively low desorption energy of $CH_3OH(s)$ (*ca.* 0.3 eV) [9]. This will promote the formation of H(s) by strengthening the dehydrogenation of CH_4 and further accelerates the L-H reaction $H(s) + H(s) \rightarrow H_2 + 2Ni(s)$. The hydrogenation reaction $CO(s) + H \rightarrow COH(s)$ leads to the formation of COH(s), which, in turn, generates CHOH(s) through further hydrogenation: $COH(s) + H \rightarrow CHOH(s)$. The formed CHOH(s) then promotes the generation of H(s) through the dehydrogenation reaction $CHOH(s) + Ni(s) \rightarrow COH(s) + H(s)$. Additionally, both the oxidative desorption reaction $CO(s) + O \rightarrow CO_2 + Ni(s)$ and the hydrogenation desorption reaction $CH_3(s) + H \rightarrow CH_4 + Ni(s)$ exhibit significant positive sensitivity coefficients due to their ability to promote the regeneration of active sites Ni(s). Fig. S7(b) shows that the hydrogenation reaction $HCOO(s) + H \rightarrow HCOOH(s)$ presents the highest negative sensitivity coefficient. The path flux analysis in Fig. 8 reveals that HCOO(s) is primarily derived from the reaction of vibrationally excited $CO_2(v)$ with H(s). Consequently, the reaction rate of $CO_2(v) + H(s) \rightarrow HCOO(s)$ decreases as the rate of the hydrogenation reaction $HCOO(s) + H \rightarrow HCOOH(s)$ decreases, which ultimately leads to an increase in the concentration of H(s).

The E-R reaction $HCOO(s) + H \rightarrow HCOOH(s)$ has the highest positive sensitivity coefficient for the formation of C₂H₄, as shown in Fig. S7(c). The desorption of HCOOH(s) can promote the regeneration of active

sites $Ni(s)$, further enhancing the generation of $CH_3(s)$ via the dissociative adsorption of CH_4. On one hand, $CH_3(s)$ can recombine to form C_2H_6 via the process $CH_3(s) + CH_3(s) \rightarrow C_2H_6 + 2Ni(s)$. The dissociation of C_2H_6 is the main formation channel of C_2H_4, as shown in Fig. S6 in the SI. On the other hand, $CH_3(s)$ can dehydrogenate on the catalyst surface to form $CH_2(s)$, which accelerates the L-H reaction $CH_2(s) + CH_2(s) \rightarrow C_2H_4(s) + Ni(s)$ and the E-R reaction $CH_2(s) + CH_2 \rightarrow C_2H_4(s)$ to form C_2H_4. Sensitivity analysis shows that the oxidation reactions $C(s) + O \rightarrow CO(s)$, $CO(s) + O \rightarrow CO_2 + Ni(s)$, as well as the formation pathway of $CH_3OH(s)$ via $CH_3(s) + O \rightarrow CH_3O(s)$, $CH_3O(s) + H \rightarrow CH_3OH(s)$ also have relatively high positive sensitivity coefficients, as they can stimulate the regeneration of active sites $Ni(s)$.

The hydrogenation reaction $CH_3(s) + H \rightarrow CH_4 + Ni(s)$ shows the largest negative sensitivity coefficient, indicating that this reaction has the strongest inhibitory effect on the formation of C_2H_4. The consumption pathway analysis of $CH_3(s)$ in Fig. 8 shows that the above-mentioned reaction has a strong competitive relationship with the dehydrogenation of $CH_3(s)$. Therefore, the reaction $CH_3(s) + H \rightarrow CH_4 + Ni(s)$ slows down the process of $CH_2(s) + CH_2(s) \rightarrow C_2H_4(s) + Ni(s)$ and $CH_2(s) + CH_2 \rightarrow C_2H_4(s)$ by inhibiting the formation of $CH_2(s)$. Meanwhile, the E-R reactions $CO(s) + H \rightarrow COH(s)$, $O(s) + H \rightarrow OH(s)$, $CO(s) + H \rightarrow HCO(s)$, $C(s) + H \rightarrow CH(s)$ directly or indirectly inhibit the desorption of $CO(s)$ to regenerate the active sites $Ni(s)$, further suppressing the generation of $CH_2(s)$, as mentioned previously.

Fig. 8 shows that the main formation pathway for $CH_3OH(s)$ is the E-R reaction $CH_3O(s) + H \rightarrow CH_3OH(s)$, while $CH_3O(s)$ is primarily formed through the oxidation reaction $CH_3(s) + O \rightarrow CH_3O(s)$. Therefore, the sensitivity analysis for CH_3OH in Fig. S7(e) indicates a strong positive sensitivity of those two reactions on the generation of CH_3OH. Due to the competition in $CH_3(s)$ consumption by the E-R reaction $CH_3(s) + H \rightarrow CH_4 + Ni(s)$ and $CH_3(s) + O \rightarrow CH_3O(s)$, the E-R reaction $CH_3(s) + H \rightarrow CH_4 + Ni(s)$ suppresses the conversion of $CH_3(s)$ to $CH_3O(s)$, thus inhibiting the formation of $CH_3OH(s)$ and CH_3OH. From Fig. S7(e), it can be observed that the hydrogenation reaction $HCOO(s) + H \rightarrow HCOOH(s)$ also presents a significant negative sensitivity coefficient. The sensitivity analysis for C_2H_6 and $HCOOH$ is also plotted and can be seen in Fig. S7.

In conclusion, Fig. S7 demonstrates that the absolute values of the sensitivity coefficients increase as the activation enthalpy introduced to each E-R reaction decreases, indicating a significant impact on the formation or consumption of each major products. Additionally, the sensitivity coefficients for H_2, C_2H_6, C_2H_4 formation are noticeably smaller compared to those of CO, CH_3OH, and $HCOOH$. This deviation in the sensitivity coefficients suggests that the influence of E-R reactions on the generation of CO, CH_3OH, and $HCOOH$ is much higher than their promotive effects on the production of H_2, C_2H_6, and C_2H_4, which is verified by the reaction path flux analysis for the aforementioned products in Fig. S6.
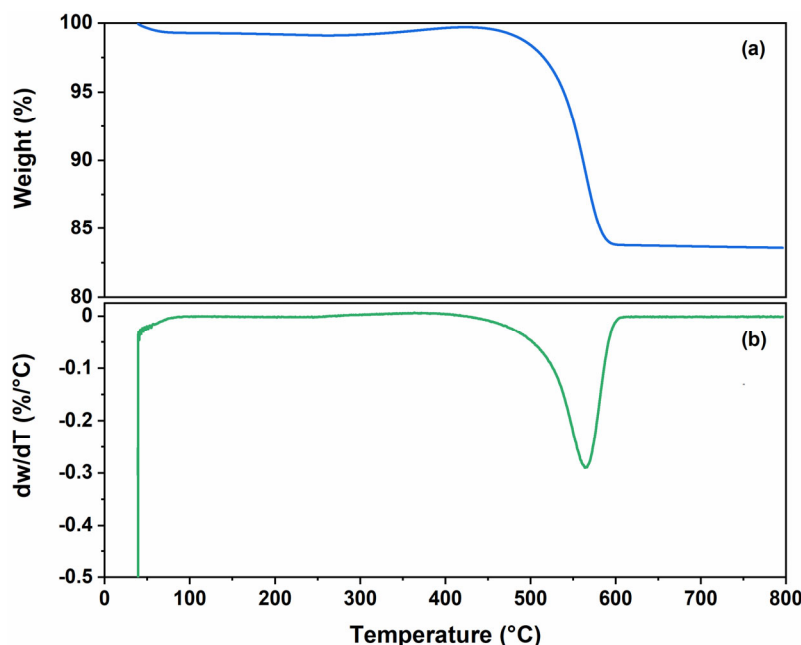
Section S.7. Carbon formation mechanism in the gas phase

Fig. S8. Analysis of carbon deposition on spent catalysts by (a) TG and (b) DTG profiles.

Thermogravimetric analysis (TGA) was performed to quantify carbon deposition of spent catalysts using a Discovery TGA55 thermogravimetric analyzer (TA, USA). The temperature was increased from 40 to 800 °C with a heating rate of 5 °C/min, in O_2 flow of 100 mL/min. Fig. S8 shows a substantial weight decline of 16.4% for the spent Ni/SiO_2 catalyst. Assuming all Ni was oxidized to nickel oxide during the TG test, the calibrated mass fraction of carbon deposition was determined to be 17.2%, suggesting a large amount of carbon deposition. The carbon species can be divided into amorphous (200~350 °C), carbon nanotubes (350~700 °C), and graphitic (> 700 °C) according to their activity and morphology [10]. From the DTG profile, the Ni/SiO_2 spent catalyst shows one main peak at 564 °C, suggesting that our deposited carbon mainly exists as carbon nanotubes [10,11].
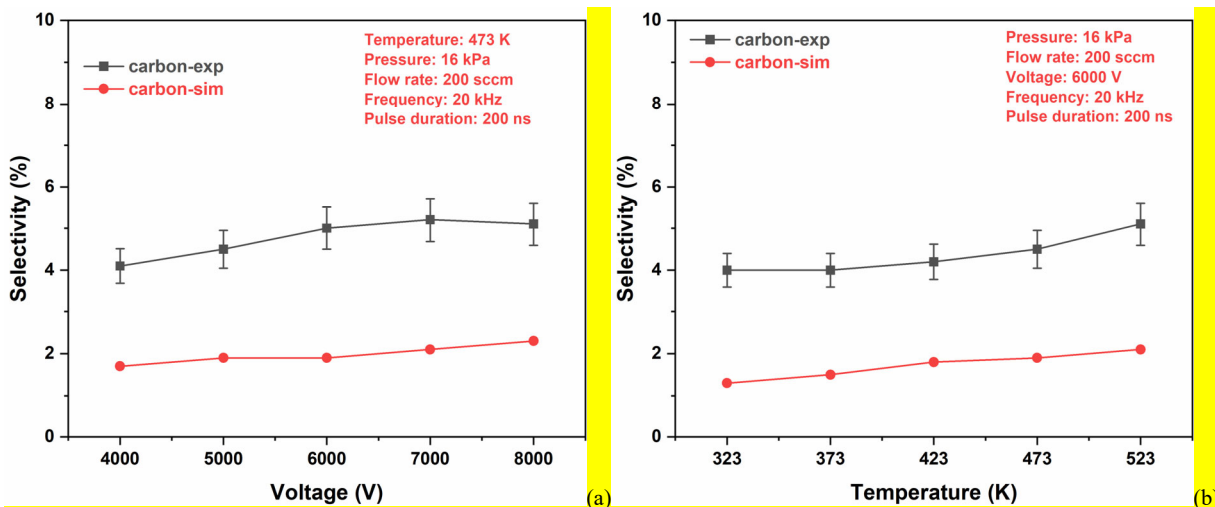

Fig. S9. Comparison of carbon deposition selectivity between experimental measurements and model predictions as a function of (a) applied voltage and (b) reaction temperature in plasma-catalytic DRM.
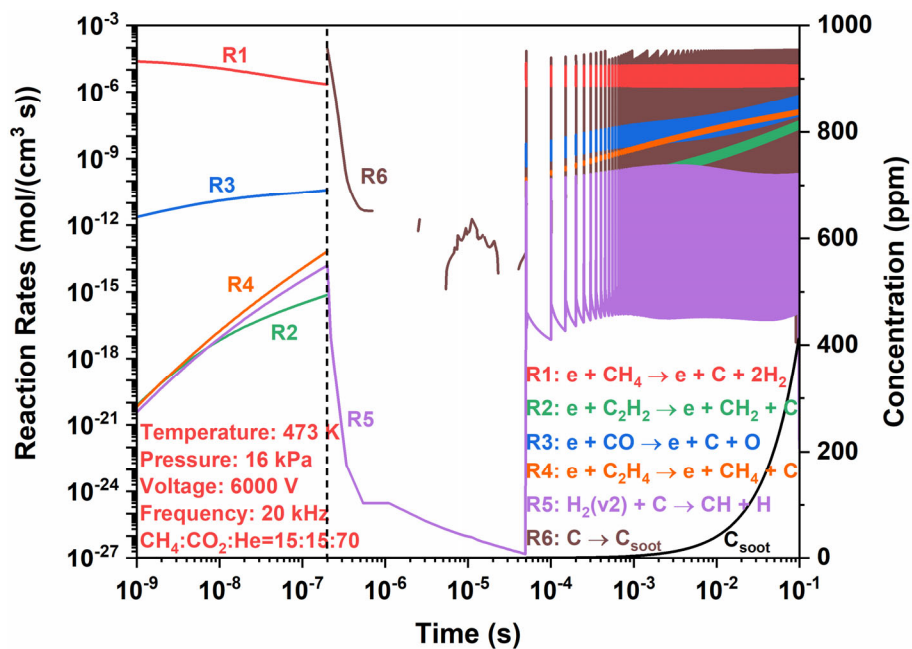
Fig. S10. Time evolution of carbon formation and consumption reactions, as well as carbon concentration, in the gas (plasma) phase, in a 0.15 CH_4/0.15 CO_2/0.70 He mixture at a pressure of 16 kPa, and temperature of 473 K.
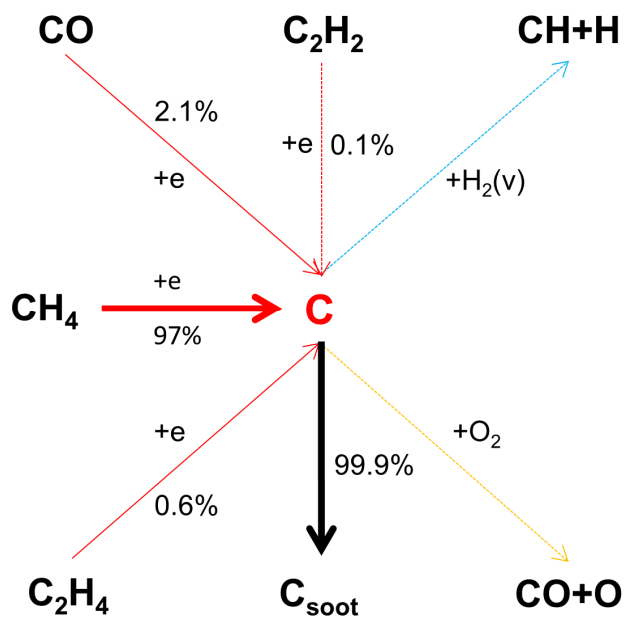

Fig. S11. Path flux analysis for carbon generated in the plasma for a 0.15 CH_4/0.15 CO_2/0.70 He mixture at a pressure of 16 kPa, and temperature of 473 K. (red lines: electron impact reaction; yellow line: chain reaction; light blue line: chain reaction accelerated by excited species; black line: deposition process)

References:

[1] Y. Yi, S. Li, Z. Cui, Y. Hao, et al., Selective oxidation of CH_4 to CH_3OH through plasma catalysis: insights from catalyst characterization and chemical kinetics modelling, *Appl. Catal. B: Environ.* 296 (2021) 120384.

https://doi.org/10.1016/j.apcatb.2021.120384

[2] B. Wanten, R. Vertongen, R. De Meyer, A. Bogaerts, Plasma-based CO_2 conversion: How to correctly analyze the performance? *J. Energy Chem*. 86 (2023) 180-196.

https://doi.org/10.1016/j.jechem.2023.07.005

[3] S. Kelly, E. Mercer, R. De Meyer, R. G. Ciocarlan, S. Bals, A. Bogaerts, Microwave plasma-based dry reforming of methane: Reaction performance and carbon formation, *J. CO2 Util.* 75 (2023) 102564.

https://doi.org/10.1016/j.jcou.2023.102564

[4] NIST Atomic Spectra Database, https://physics.nist.gov/PhysRefData/ASD/lines_form.html

[5] P.G. Reyes, A. Gómez, J. Vergara, H. Martinez, C. Torres, Plasma diagnostics of glow discharges in mixtures of CO_2 with noble gases, *Rev. Mex. Fis.* 63 (2017) 363-371.

[6] Y. Wang, Y. Chen, J. Harding, H. He, A. Bogaerts, X. Tu, Catalyst-free single-step plasma reforming of CH_4 and CO_2 to higher value oxygenates under ambient conditions, *Chem. Eng. J.* 450 (2022) 137860.

https://doi.org/10.1016/j.cej.2022.137860

[7] L. Dou, Y. Liu, Y. Gao, J. Li, X. Hu, S. Zhang, K. Ostrikov, T. Shao, Disentangling metallic cobalt sites and oxygen vacancy effects in synergistic plasma-catalytic CO2/CH4 conversion into oxygenates, *Appl. Catal. B: Environ.* 318 (2022) 121830.

https://doi.org/10.1016/j.apcatb.2022.121830

[8] J. Sun, Q. Chen, X. Zhao, H. Lin, W. Qin, Kinetic investigation of plasma catalytic synthesis of ammonia: insights into the role of excited states and plasma-enhanced surface chemistry, *Plasma Sources Sci. Technol.* 31 (2022) 094009.

https://doi.org/10.1088/1361-6595/ac8e2c

[9] Y. A. Zhu, D. Chen, X. G. Zhou, W. K. Yuan, DFT studies of dry reforming of methane on Ni catalyst, *Catal. Today* 148 (2008) 260-267.

https://doi.org/10.1016/j.cattod.2009.08.022

[10] Y. Gao, A. Aihemaiti, J. Jiang, Y. Meng, T. Ju, S. Han, X. Chen, J. Liu, Inspection over carbon deposition features of various nickel catalysts during simulated biogas dry reforming, *J. Clean. Prod.* 260 (2020) 120944.

https://doi.org/10.1016/j.jclepro.2020.120944

[11] V. Pawar, D. Ray, C. Subrahmanyam, V. M. Janardhanan, Study of short-term catalyst deactivation due to carbon deposition during biogas dry reforming on supported Ni catalyst, *Energy Fuels* 29 (2015) 8047-8052.

https://doi.org/10.1021/acs.energyfuels.5b01862